

**A MEASUREMENT OF THE  $e^+e^-$  DECAY WIDTH  
OF THE  $Z^0$**

John Michael Yamartino

SLAC-Report-426  
February 1994

Prepared for the Department of Energy  
under contract number DE-AC03-76SF00515

SLAC-426  
UC-414  
(E)

**A Measurement of the  $e^+e^-$   
Decay Width of the  $Z^0$  \***

**John Michael Yamartino**

Stanford Linear Accelerator Center  
Stanford University  
Stanford, California 94309

February 1994

Prepared for the Department of Energy  
under contract number DE-AC03-76SF00515

Printed in the United States of America. Available from the National  
Technical Information Service, U.S. Department of Commerce,  
5285 Port Royal Road, Springfield, Virginia 22161.

---

\* Ph.D. thesis, Massachusetts Institute of Technology

## Abstract

This thesis presents a measurement of the partial decay width of the  $Z^0$  to  $e^+e^-$  using data recorded by the SLD at the SLAC Linear Collider during the 1992 run. Based on  $354 \text{ nb}^{-1}$  of data, the decay width,  $\Gamma_{ee}$  is measured to be  $82.4 \pm \text{}^{3.6}_{3.7} \pm 0.8 \text{ MeV}$  where the first error is statistical and the second is systematic. By combining this measurement of  $\Gamma_{ee}$  with the SLD measurement of  $A_{LR}$ , the magnitude of the effective vector and axial-vector coupling constants of the electron,  $\overline{g}_v^e$  and  $\overline{g}_a^e$ , are determined to be  $0.024 \pm 0.011$  and  $0.498 \pm 0.011$  respectively.

## Acknowledgments

One of the highlights of my graduate career is to have been a student in the Counter Spark Chamber group. I feel privileged to know such a nice group of physicists and wish to thank Wit Busza, Jerry Friedman, Henry Kendall, Louis Osborne, Larry Rosenson, Frank Taylor and Robin Verrier for all that they have offered me. In particular I would like to thank my advisor Larry Rosenson for his guidance and friendship.

I also wish to thank the group's administrative assistant, Sandy Fowler, for all of her help particularly while I was at SLAC. I would like to extend the same thanks to Peggy Berkovitz in the Physics Graduate Office.

This work would not have been possible were it not for the efforts of many people who contributed to the construction and operation of the SLC and the SLD. I would like to thank them and wish them continued and greater successes.

In particular I would like to thank Kevin Pitts for his analysis of the integrated luminosity. I would also like to thank Saúl González for starting the PAW revolution on the SLD and David C. Williams for helping me whenever I needed to get out of a computer jam. Their efforts have made significant contributions to my work.

I thank Mark Baker for his TeX help with this document. I would also like to thank Sarah Hedges, Bruce Schumm and Saúl González for proofreading this thesis.

I would like to express my thanks to my fellow graduate students Saúl González, Amit Lath and David (and Suzanne) Williams for their friendship. I take comfort in knowing that high energy physics will keep us in touch and bring us together even though we may live far apart. I have made friends with many others who inhabit the halls of the Central Lab Annex. I thank them for their friendship and only regret that I could not have worked directly with all of them. I would also like to thank the WIC group and others involved with the WIC construction and commissioning. It was a

pleasure to work with them. Thanks also to Phil Burrows, Traudl Hansl-Kozanecka and Uwe Schneekloth of the MIT contingent here at SLAC.

Although I made no discoveries in the SLD data, I have made the discovery of a lifetime among the people of California. My wife Andrea has been a great companion for me. She has provided the most important kind of support in these last few months of my thesis work.

This thesis is dedicated to my wife and my family who have given me everything that I really need.

... in the practice of science, indeed in all scholarly pursuits and, in some sense, even in everyday life, one must strike a delicate balance between two opposing forces - respect for the authority of past achievements and the confidence in one's own independent creativity.

*Hans Christian von Bayer*

# Contents

<b>1</b>	<b>Introduction</b>	<b>14</b>
1.1	Thesis Overview . . . . .	14
1.2	The Standard Model of Electroweak Interactions . . . . .	15
1.2.1	Gauge Bosons . . . . .	15
1.2.2	Fermions . . . . .	19
1.2.3	Weak Neutral Coupling Constants . . . . .	20
1.3	The Fundamental Constants of the Electroweak Theory . . . . .	21
1.4	Radiative Corrections . . . . .	22
1.5	Partial Decay Rates of the $Z^0$ . . . . .	23
1.6	Parity Violation in the $Z_{f\bar{f}}$ Couplings . . . . .	25
1.7	Extracting $\bar{g}_v^e$ and $\bar{g}_a^e$ with $A_{LR}$ and $\Gamma_{ee}$ . . . . .	27
<b>2</b>	<b>Bhabha Scattering at the <math>Z^0</math></b>	<b>30</b>
2.1	Lowest Order Bhabha Cross Section . . . . .	30
2.2	Sensitivity of $\sigma_{ee}$ to $\Gamma_{ee}$ . . . . .	33

2.3	Model Independent Bhabha Approximation . . . . .	35
<b>3</b>	<b>The SLC and the SLD</b>	<b>38</b>
3.1	The SLAC Linear Collider . . . . .	38
3.2	The SLC Large Detector . . . . .	41
3.2.1	Tracking . . . . .	42
3.2.2	Particle Identification . . . . .	45
3.2.3	Calorimetry . . . . .	46
3.2.4	Luminosity Monitor . . . . .	51
3.3	Simulation . . . . .	54
<b>4</b>	<b>Triggering and Event Selection</b>	<b>57</b>
4.1	Backgrounds and Triggering Strategy . . . . .	57
4.1.1	SLC $\mu$ Background . . . . .	57
4.1.2	Trigger Algorithm . . . . .	59
4.2	PASS 1 Selection . . . . .	61
4.3	Reconstruction and Energy Scale . . . . .	64
4.3.1	Clustering . . . . .	64
4.3.2	Energy Scale . . . . .	64
4.3.3	$\pi^0$ Mass Reconstruction . . . . .	65
4.4	LAC Response to Bhabha and Hadronic events . . . . .	67
4.4.1	Selection . . . . .	68



4.4.2	Polar Angle Features of the LAC Response . . . . .	68
4.5	Selecting Wide Angle Bhabha Events . . . . .	71
4.5.1	Fiducial Definition . . . . .	71
4.5.2	Cluster Selection . . . . .	72
4.5.3	Event Selection . . . . .	73
4.5.4	Comparison with Monte Carlo . . . . .	73
<b>5</b>	<b>The Wide Angle Bhabha Cross Section</b>	<b>78</b>
5.1	The Cross Section . . . . .	78
5.2	Corrections to the Wide Angle Bhabha Yield . . . . .	79
5.2.1	Efficiency . . . . .	79
5.2.2	Backgrounds . . . . .	85
5.2.3	Beam Energy Spread . . . . .	86
5.3	Integrated Luminosity . . . . .	89
5.4	The Measured Cross Section . . . . .	91
<b>6</b>	<b>Results</b>	<b>93</b>
6.1	$\Gamma_{ee}$ . . . . .	93
6.1.1	Cross Section Fit to $\Gamma_{ee}$ . . . . .	94
6.1.2	Systematic Errors . . . . .	95
6.2	Comparison with LEP . . . . .	97
6.3	$\bar{g}_v^e$ and $\bar{g}_a^e$ . . . . .	97

6.4	Summary of Results . . . . .	98
6.5	Prospects . . . . .	100
<b>A</b>	<b>SLC Muon Pattern Recognition</b>	<b>102</b>
A.1	The Algorithm . . . . .	102

# List of Figures

1-1	Feynman diagrams for $e^+e^-$ annihilation. . . . .	17
1-2	The cross section for $e^+e^- \rightarrow \mu^+\mu^-$ . . . . .	17
1-3	Feynman diagrams for the neutral current interactions. . . . .	18
1-4	Examples of QED radiative corrections. . . . .	23
1-5	Electroweak radiative corrections to $e^+e^- \rightarrow Z^0 \rightarrow f\bar{f}$ . . . . .	24
1-6	$\Gamma_{ee}$ and $A_{LR}$ in the vector – axial-vector plane. . . . .	28
2-1	Feynman diagrams for Bhabha scattering to lowest order. . . . .	31
2-2	The wide angle Bhabha cross section vs. $\cos \theta_s$ . . . . .	32
2-3	The Sensitivity function $S(\Gamma_{ee})$ vs. $\cos \theta_s$ . . . . .	34
2-4	The theoretical dependance of $\sigma_{ee}$ on $\Gamma_{ee}$ . . . . .	37
3-1	The layout of the SLAC Linear Collider. . . . .	39
3-2	Schematic design of the extraction-line spectrometer. . . . .	41
3-3	The Compton polarimeter system. . . . .	42
3-4	A cutaway view of the SLD. . . . .	43

3-5	A quadrant view of the SLD. . . . .	44
3-6	The CCD vertex detector. . . . .	45
3-7	A view of a barrel CRID sector. . . . .	47
3-8	Two cells of the LAC. . . . .	48
3-9	LAC barrel modules. . . . .	49
3-10	An assembly drawing of the LAC barrel. . . . .	50
3-11	A side view of the LMSAT. . . . .	52
3-12	A face on view of the LMSAT. . . . .	53
3-13	A display of a $Z^0 \rightarrow \tau^+\tau^-\gamma$ event. . . . .	54
4-1	Display of LAC hits for a luminosity Bhabha event. . . . .	58
4-2	The number of $\mu$ 's in the LAC per small angle Bhabha event. . . . .	59
4-3	ADC spectra for $\mu$ induced clusters in the LAC barrel. . . . .	60
4-4	PASS 1 Events. . . . .	63
4-5	$\gamma\gamma$ invariant mass distribution. . . . .	67
4-6	$I_{mb}$ for all PASS 1 Events. . . . .	69
4-7	$E_{Raw}$ vs. $ \cos \theta_1 $ . . . . .	70
4-8	$E_{totEM}$ vs. $N_{good}$ . . . . .	74
4-9	$N_{good}$ for fiducial events. . . . .	75
4-10	$E_{totEM}$ for low multiplicity fiducial events . . . . .	76
4-11	$E_{totEM}$ for selected wide angle Bhabha events . . . . .	77

5-1	ENERGY trigger quantities for fiducial Monte Carlo $e^+e^-$ events. . .	80
5-2	PASS 1 selection cuts for <i>fiducial</i> Monte Carlo $e^+e^-$ events. . . . .	82
5-3	The trigger quantities EHI and ELO for selected events. . . . .	83
5-4	$E_{totEM}$ for all events which pass the PASS 1 cuts. . . . .	84
5-5	$N_{good}$ for all events which pass the PASS 1 cuts. . . . .	85
5-6	$\Theta_{acol}$ for events which pass all other cuts. . . . .	86
5-7	The Cross Section for $e^+e^-$ events into the fiducial region. . . . .	87
5-8	The center of mass energy distribution for the SLC. . . . .	88
6-1	The theoretical dependance of the cross section on $\Gamma_{ee}$ . . . . .	94
6-2	The measured cross section projected onto the theoretical curve. . . .	95
6-3	The errors to the theoretical curve. . . . .	96
6-4	The 1-sigma contours of $\bar{g}_v^e$ and $\bar{g}_a^e$ from $\Gamma_{ee}$ and $A_{LR}$ . . . . .	99
A-1	$n_t$ vs. $n_l$ for coarse clusters. . . . .	105
A-2	$n_t$ vs. $n_l$ for refined clusters. . . . .	106
A-3	$n_t$ vs. $n_l$ for coarse clusters in LMSAT events. . . . .	107
A-4	A display of a hadronic event after SLC muon removal. . . . .	108
A-5	A display of identified SLC muon induced clusters. . . . .	108

# List of Tables

1.1	The axial-vector and vector coupling constants, $g_a^f$ and $g_v^f$ . . . . .	21
1.2	The Fundamental Constants of the Electroweak Theory . . . . .	21
1.3	The value of Left-Right asymmetry, $A_f$ , for each fermion type . . . .	26
5.1	Efficiencies for detecting and identifying wide angle Bhabhas. . . . .	85
5.2	The expected number of background events from different processes. .	86
5.3	The systematic errors in the measurement of the cross section. . . . .	92
6.1	The systematic errors in the measurement of the $\Gamma_{ee}$ . . . . .	96
6.2	Recent results from LEP for $\Gamma_{ee}$ . . . . .	97

# Chapter 1

## Introduction

This thesis will present a measurement of the  $e^+e^-$  decay width of the  $Z^0$  ( $\Gamma_{ee}$ ).

The measurement presented here is one of only a handful of measurements to come exclusively from the first physics run of the SLD experiment. That run occurred in 1992 and represented the first time that  $Z^0$  events were produced with a longitudinally polarized electron beams. This measurement does not make use of the polarization of the electron beam. The polarization was used, however, to make the first measurement of the Left-Right polarization cross section asymmetry ( $A_{LR}$ ) [1]. A measurement of  $\Gamma_{ee}$  reveals information about the weak neutral coupling constants which is complementary to that from  $A_{LR}$ .

### 1.1 Thesis Overview

The remaining sections of this chapter will discuss the Standard Model of Electroweak Interactions and some fundamental measurements of the  $Z^0$ . Chapter 2 will discuss the theory of Bhabha ( $e^+e^- \rightarrow e^+e^-$ ) scattering at the  $Z^0$ . Chapter 3 will describe the SLAC Linear Collider (SLC) and the SLD Large Detector (SLD). Chapter 4 will

describe the triggering and event selection. Chapter 5 will describe the cross section measurement and Chapter 6 will give the final result for  $\Gamma_{ee}$  and the weak neutral couplings.

## 1.2 The Standard Model of Electroweak Interactions

During the 1960's, Glashow, Weinberg and Salam [2][3][4] developed a theory which unified the Weak and Electromagnetic interactions into a single 'Electroweak' interaction. The interaction theory describes the forces between the constituents of matter. These constituents are known as *fermions* and are spin one-half, point like particles. The mediators of the force are known as *bosons* and are integral spin, gauge particles.

This theory has come to be known as the "Standard model of Electroweak Interactions". It is a gauge theory based on Group  $SU(2)_L \times U(1)$ . The  $SU(2)_L$  is a weak isospin group with a  $V - A$  structure which only couples to the left-handed fermions. The  $U(1)$  is the electromagnetic group which couples to the right- and left-handed fermions. The fields are mixed in the theory with a parameter known as the weak mixing angle  $\theta_w$ .

### 1.2.1 Gauge Bosons

The electromagnetic vector field, denoted as  $B_\mu$ , and the weak isotriplet of vector fields, denoted as  $W_\mu^i$  are mixed to form the four fields

$$\begin{aligned} W^\pm &= \sqrt{\frac{1}{2}}(W^1 \pm W^2) \\ Z_\mu &= B_\mu \cos \theta_w + W_\mu^3 \sin \theta_w \end{aligned}$$



$$A_\mu = -B_\mu \cos \theta_w + W_\mu^3 \sin \theta_w$$

which correspond to the  $W^\pm$ ,  $Z^0$ , and  $\gamma$  gauge bosons respectively. The mass of the  $W$ ,  $M_W$ , is related to the mass of the  $Z^0$ ,  $M_Z$ , through the following relation:

$$M_W = M_Z \cos \theta_w. \quad (1.1)$$

The  $\gamma$  is massless.

The exchange of a  $W^+$  or a  $W^-$  boson is known as the charged current interaction and an exchange of a  $\gamma$  or a  $Z^0$  is known as the neutral current interaction. The charged current interactions are not involved in the process  $e^+e^- \rightarrow f\bar{f}$  at the  $Z^0$  resonance energies as, strictly speaking, the contributions are small. We will now consider only the neutral current interactions.

The Feynman diagrams for the reaction  $e^+e^- \rightarrow f\bar{f}$ , where  $f$  represents a fermion (to be discussed in the following subsection) are shown in Figure 1-1. The more complicated case where  $f$  is an electron will be discussed in Chapter 2.

Since the  $Z^0$  is massive, the cross section for  $e^+e^- \rightarrow f\bar{f}$  will go through a resonance when the center of mass energy,  $E_{cm}$ , is near  $M_Z$ . This can be seen in Figure 1-2 which is generated by evaluating the graphs in Figure 1-1 for the case where  $f = \mu$ .

The Feynman (vertex) diagrams for the neutral current interactions are shown in Figure 1-3. The coupling  $e$  is the unit of charge equal to that of the positron. It is related to the fine structure constant by the following relation:

$$\alpha = \frac{e^2}{4\pi} \quad (1.2)$$

$Q_f$  is the charge of the fermion in units of  $e$ . The “weak” charge, denoted by

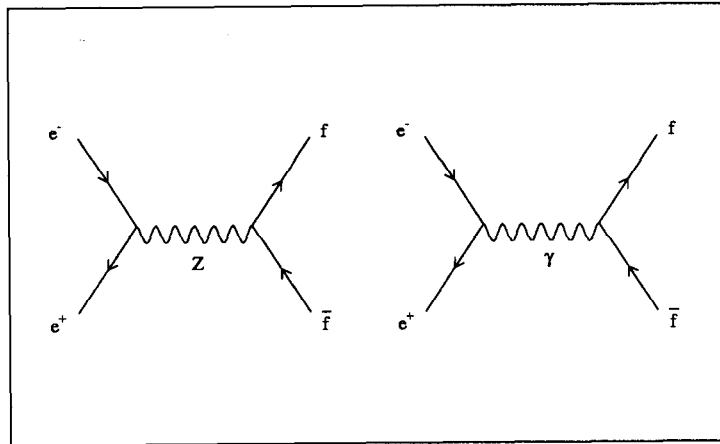


Figure 1-1: Feynman diagrams for  $e^+e^-$  annihilation.

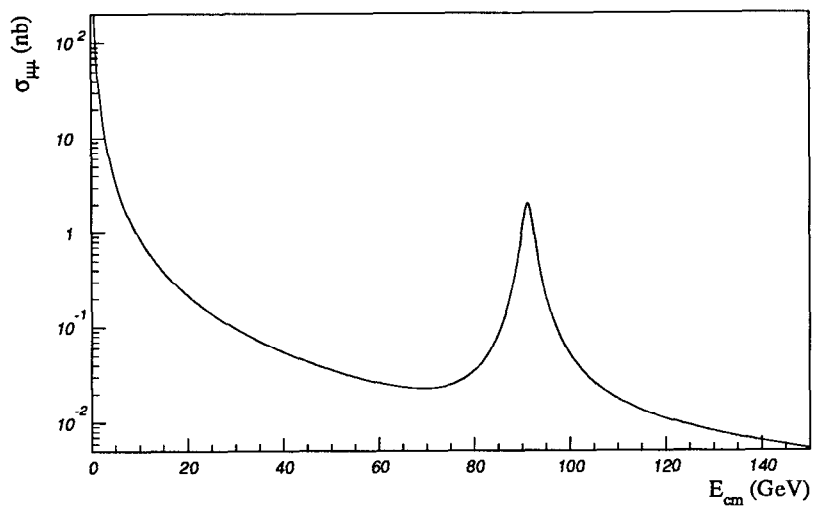
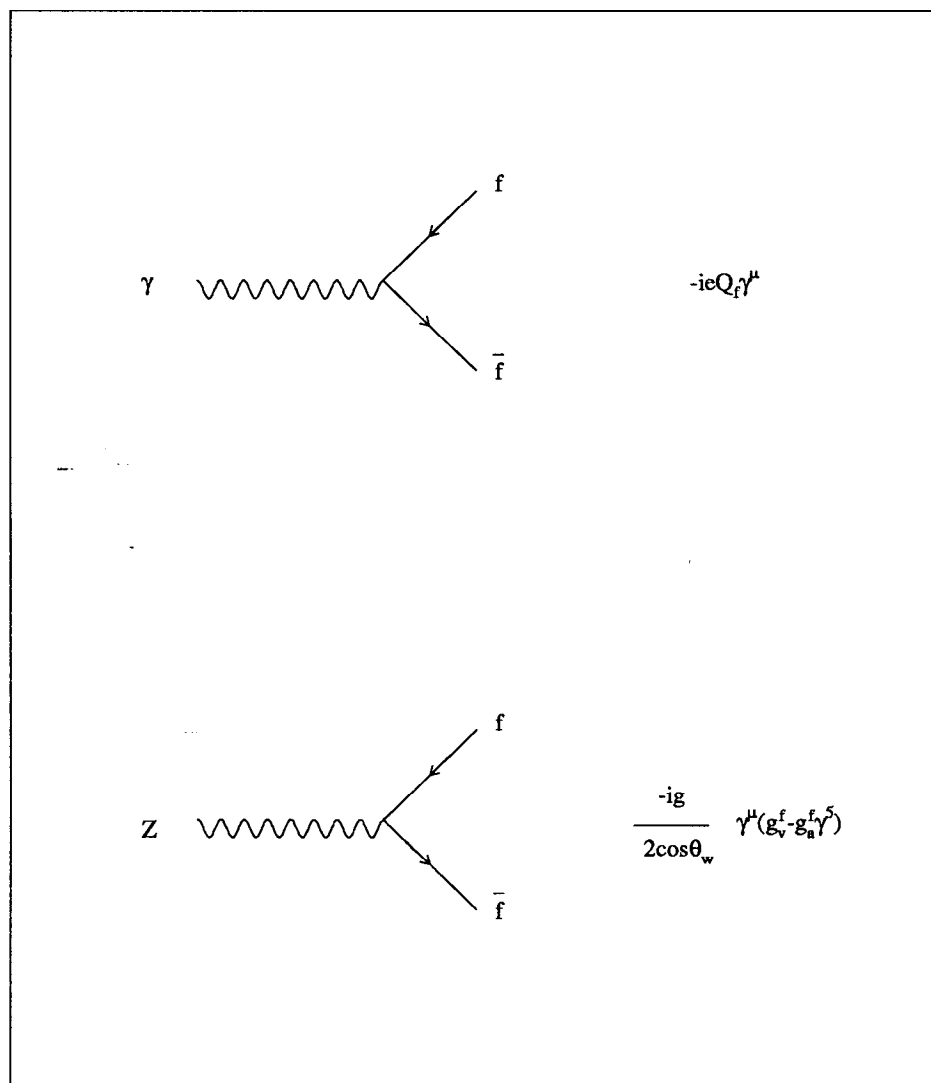


Figure 1-2: The cross section for  $e^+e^- \rightarrow \mu^+\mu^-$ .



**Figure 1-3:** Feynman diagrams and vertex factors for the neutral current interactions.

$g$ , represents the strength of the weak couplings. From low energy weak interaction theory  $g$  is related to the Fermi constant,  $G_F$ , and  $M_W$  in the following way:

$$\frac{G_F}{\sqrt{2}} = \frac{g^2}{8M_W^2}. \quad (1.3)$$

The unification condition is such that  $e = g \sin \theta_w$ .

The vector and axial-vector coupling constants are denoted as  $g_v^f$  and  $g_a^f$  respectively. These will be discussed in a later subsection.

### 1.2.2 Fermions

In the Standard Model there are two classes of fermions, quarks and leptons. Pairs of quarks and pairs of leptons are arranged into three generations of left-handed weak isodoublets.

$$\begin{pmatrix} u \\ d \end{pmatrix}_L \quad \begin{pmatrix} c \\ s \end{pmatrix}_L \quad \begin{pmatrix} t \\ b \end{pmatrix}_L$$

$$\begin{pmatrix} \nu_e \\ e \end{pmatrix}_L \quad \begin{pmatrix} \nu_\mu \\ \mu \end{pmatrix}_L \quad \begin{pmatrix} \nu_\tau \\ \tau \end{pmatrix}_L$$

The quarks are the upper set of isodoublets and the leptons are the lower set of isodoublets. The quarks have charge  $Q_f = +\frac{2}{3}$  for  $f = u, c, t$  and  $Q_f = -\frac{1}{3}$  for  $f = d, s, b$ . The neutrinos ( $\nu$ ) are charge neutral and the  $e, \mu, \tau$  leptons have charge  $Q_f = -1$ . All fermions have an anti-particle partner which has the same mass, opposite charge and handedness. The other quantum number which is opposite for

antiparticles is the *flavor* of the fermion which is denoted by the letter that symbolizes the fermion. Flavor is a quantum number which is conserved in neutral current interactions.

The third component of the weak isospin  $T_f^3$  is  $+\frac{1}{2}$  for the upper element of the isodoublet and  $-\frac{1}{2}$  for the lower element. All fermions are right-handed isosinglets with weak isospin 0. This implies that right handed neutrinos do not couple to the electroweak field.

Neither the  $\tau$  neutrino nor the  $t$  quark have been observed *directly*. However, both the  $\tau$  lepton and the  $b$  quark have been determined experimentally to belong to an isodoublet ( $|T_f^3| \sim \frac{1}{2}$ ), implying the existence of their isodoublet partner.

## Mass

The Electroweak theory requires the existence of some mechanism which generates mass for the  $W^\pm$  and  $Z^0$  bosons. The Higgs mechanism of spontaneous symmetry breaking is introduced for this purpose. The simplest version of the Higgs mechanism is as a scalar Higgs field. The Higgs field is also responsible for the mass of the fermions. The Higgs boson (the gauge boson of the Higgs field) has not yet been observed nor has the gauge boson of any other possible field responsible for spontaneous symmetry breaking.

### 1.2.3 Weak Neutral Coupling Constants

In the Standard Model, the weak neutral couplings,  $g_v^f$ , and  $g_a^f$  have the following form.

$$g_v^f = T_f^3 - 2Q_f \sin^2 \theta_w$$

$$g_a^f = T_f^3$$

The  $g_v^f$  and  $g_a^f$  couplings are shown in Table 1.1.

fermion type	$g_a^f$	$g_v^f$ for $\sin^2 \theta_w = 0.23$
$\nu_e, \nu_\mu, \nu_\tau$	$\frac{1}{2}$	$\frac{1}{2}$
$e^-, \mu^-, \tau^-$	$-\frac{1}{2}$	$-\frac{1}{2} + 2 \sin^2 \theta_w \simeq -0.04$
$u, c, t$	$\frac{1}{2}$	$\frac{1}{2} - \frac{4}{3} \sin^2 \theta_w \simeq 0.19$
$d, s, b$	$-\frac{1}{2}$	$-\frac{1}{2} + \frac{2}{3} \sin^2 \theta_w \simeq -0.35$

**Table 1.1:** The axial-vector and vector coupling constants,  $g_a^f$  and  $g_v^f$ .

## 1.3 The Fundamental Constants of the Electroweak Theory

The previous sections have discussed the structure of the electroweak theory. The coupling strength of the theory is completely (though not uniquely) constrained by the parameters  $\alpha$ ,  $G_F$ , and  $M_Z$ . The constant  $\alpha$ , can be thought of as the strength of the 'electromagnetic' ( $U(1)$ ) part of the theory (see eq. (1.2)), the constant  $G_F$ , can be thought of as the strength of the 'weak' ( $SU(2)_L$ ) part of the theory (see eq. (1.3)), and  $M_Z$  can be thought of as a measure of the degree to which the 'electromagnetic' and 'weak' parts mix (see eq. (1.1)).

The value of fundamental constants  $\alpha$ ,  $G_F$ , and  $M_Z$  are given in Table 1.2.

parameter	measured value	precision (ppm)
$\alpha$ [5]	$(137.0359895(61))^{-1}$	0.045
$G_F$ [5]	$1.16639(2) \times 10^{-5} \text{ GeV}^{-2}$	17
$M_Z$ [6]	91.187(7) GeV	77

**Table 1.2:** The Fundamental Constants of the Electroweak Theory

## 1.4 Radiative Corrections

Below we will give a brief discussion of radiative corrections that are important in  $e^+e^-$  annihilation at the  $Z^0$ . A more thorough discussion can be found in reference [7].

### QED Radiative Corrections

There are two types of QED radiative corrections. These are *real*, which correspond to the emission of a real photon, and *virtual* which correspond to emission and reabsorption of virtual photons (see Figure 1-4).

The most important real QED correction to  $e^+e^- \rightarrow Z^0 \rightarrow f\bar{f}$  is that for initial state radiation. This reduces the peak cross section by  $\sim 30\%$  and shifts the peak by  $\sim 100$  MeV. Final state radiation has a much smaller effect on the line shape but does effects the topology of the event (the acolinearity of the final state  $f\bar{f}$  for example, or the cluster multiplicity in a low multiplicity event).

An important virtual QED correction is the running of  $\alpha$  to  $q^2 = M_Z^2$  which results from reduced screening of the bare electron charge. This changes  $\alpha^{-1}$  from  $\sim 137$  at  $q^2 = 0$  to  $\sim 128$  at  $q^2 = M_Z^2$ .

The QED corrections will be made to the theory so that it can be directly compared with the experimental results.

### Electroweak Radiative Corrections

Electroweak radiative corrections involve exchange of, and/or loops of fermions and bosons, and can be divided into three categories. They are known as loop corrections, vertex correction and box diagram corrections (see Figure 1-5). The latter has been shown to be negligibly small. The loop and vertex corrections have dependences on the yet unobserved  $t$  quark and the Higgs boson. They effect  $\Gamma_{ee}$  at the sub-1% level.

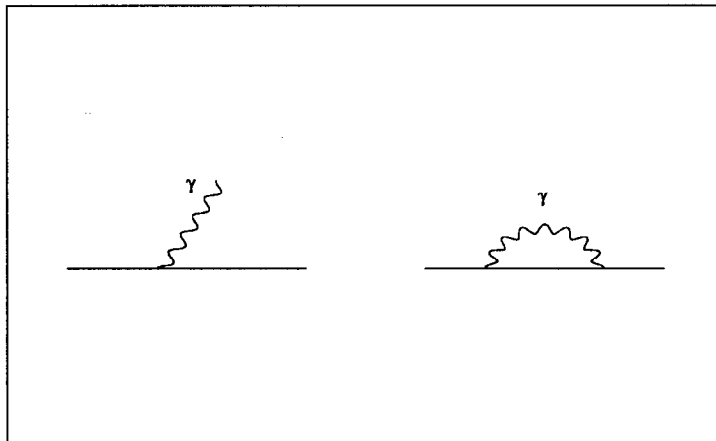


**Figure 1-4:** Examples of QED radiative corrections. An example of a real correction (left) and a virtual correction (right).

It is possible to set limits on the masses of the  $t$  quark and the Higgs boson with precision electroweak measurements using the radiative corrections.

The effects of the electroweak radiative corrections will be absorbed into the observables and will be compared with the measured observables.

## 1.5 Partial Decay Rates of the $Z^0$

The  $Z^0$  can decay into any fermion – anti-fermion pair. From the vertex factor in Figure 1-3 and eq. (1.3) the decay rate  $\Gamma_{f\bar{f}}$  (also known as the decay width or partial width) for  $Z^0 \rightarrow f\bar{f}$  is

$$\Gamma_{f\bar{f}} = \frac{G_F M_Z^3}{6\sqrt{2}\pi} (g_v^{f^2} + g_a^{f^2}) \cdot C_f, \quad (1.4)$$



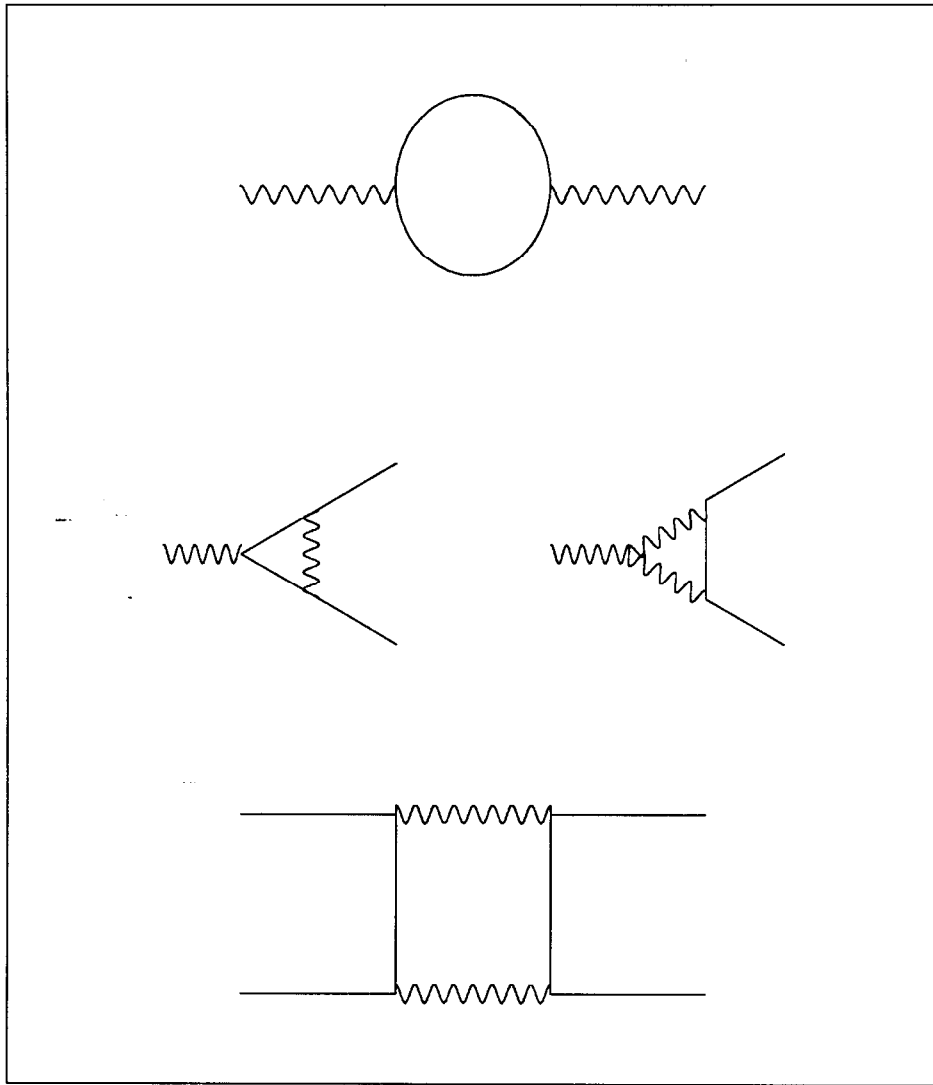


**Figure 1-5:** Electroweak radiative corrections to  $e^+e^- \rightarrow Z^0 \rightarrow f\bar{f}$ . The solid lines are fermions and the curvy lines represent  $\gamma$ ,  $Z^0$  and (where appropriate)  $W^\pm$  bosons. The top graph is an example of a loop correction, the middle are vertex corrections and the bottom a box diagram.

where  $C_f$  is the combined color factor and QCD correction which is 1 for leptons and  $3(1 + \alpha_s/\pi)$  for quarks.

This is known as the tree level expression for  $\Gamma_{f\bar{f}}$ . Using the constants in Table 1.1 and Table 1.2,  $\Gamma_{ee} = 83.47$  MeV.

When higher order corrections such as vertex corrections and loop corrections are absorbed into  $g_v^f$  and  $g_a^f$  the couplings are then referred to as “effective” coupling constants. The effective couplings are denoted with a bar over the  $g$  such as  $\bar{g}_v^f$  and  $\bar{g}_a^f$  as opposed to  $g_v^f$  and  $g_a^f$  which denote the “bare” couplings.

## 1.6 Parity Violation in the $Z_{f\bar{f}}$ Couplings

The  $Z^0$  couples to left- and right-handed fermions with different strengths (from vertex factor in Figure 1-3). This can be demonstrated by rewriting the  $V - A$  part of the vertex factor as follows:

$$g_v^f - g_a^f \gamma^5 = g_R^f (1 + \gamma^5) + g_L^f (1 - \gamma^5)$$

where

$$g_R^f = \frac{1}{2}(g_v^f - g_a^f)$$

$$g_L^f = \frac{1}{2}(g_v^f + g_a^f).$$

The asymmetry of the couplings, denoted as  $A_f$ , is then defined as follows:

$$A_f = \frac{g_L^{f^2} - g_R^{f^2}}{g_L^{f^2} + g_R^{f^2}}$$

which reduces to

$$A_f = \frac{2g_a^f g_v^f}{g_v^{f^2} + g_a^{f^2}}. \quad (1.5)$$

The expected values of  $A_f$  for each fermion type is given in Table 1.3.

fermion type	$A_f$
$\nu_e, \nu_\mu, \nu_\tau$	1
$e^-, \mu^-, \tau^-$	0.16
$u, c, t$	0.66
$d, s, b$	0.94

**Table 1.3:** The value of Left-Right asymmetry,  $A_f$ , for each fermion type

The Left-Right polarization cross section asymmetry,  $A_{LR}$ , for  $e^+e^-$  annihilation at the  $Z^0$  resonance, defined as follows:

$$A_{LR} = \frac{\sigma_L - \sigma_R}{\sigma_L + \sigma_R},$$

is equal to  $A_f$  for the electron,  $A_e$ .  $A_{LR}$  is measured by colliding longitudinally polarized electrons with (unpolarized or polarized) positrons at the  $Z^0$  resonance and measuring the asymmetry in the cross section between events produced with the electrons in the left-handed state and those produced in the right handed state.

Eq.(1.5) is also the tree level expression for  $A_f$ . If the measurement of  $A_{LR}$  (corrected for initial state QED effects) is equated to the right side of eq.(1.5) then

the couplings are considered to be effective in the same sense that was described earlier for the partial width.

$A_f$  for other fermion types can be measured using the polar angular distribution for the final state  $f$  in  $e^+e^-$  annihilation produced with a polarized electron beam [8].

## 1.7 Extracting $\bar{g}_v^e$ and $\bar{g}_a^e$ with $A_{LR}$ and $\Gamma_{ee}$

Once the partial widths and asymmetries have been measured it is possible to extract the effective vector and axial-vector coupling constants  $\bar{g}_v^e$  and  $\bar{g}_a^e$ . Given the expressions for  $\Gamma_{ee}$ , eq.(1.4) for electrons, and the expression for  $A_{LR}$ , eq.(1.5), one can solve the equations for  $\bar{g}_v^e$  and  $\bar{g}_a^e$ .

Figure 1-6 shows the vector – axial-vector plane with the expression for  $\Gamma_{ee}$  and  $A_{LR}$  shown. The solution for  $\Gamma_{ee}$  is represented as a circle, while solutions for  $A_{LR}$  are represented as two lines. The dashed line represents the case where the vector coupling is dominant (i.e.  $\bar{g}_v^e$  is large and  $\bar{g}_a^e$  is small). Since we know that the electron and  $\nu_e$  belong to an isodoublet, this solution can be excluded.

The solid line and the circle intersect at two points given by:

$$\bar{g}_v^e \cong \pm \sqrt{\frac{\Gamma_{ee}}{C_{SM}}} \frac{A_{LR}}{2} \quad (1.6)$$

$$\bar{g}_a^e \cong \pm \sqrt{\frac{\Gamma_{ee}}{C_{SM}}} \quad (1.7)$$

where the approximation is for the case that  $A_{LR}^2 \ll 1$ .

$C_{SM}$  is defined as follows:

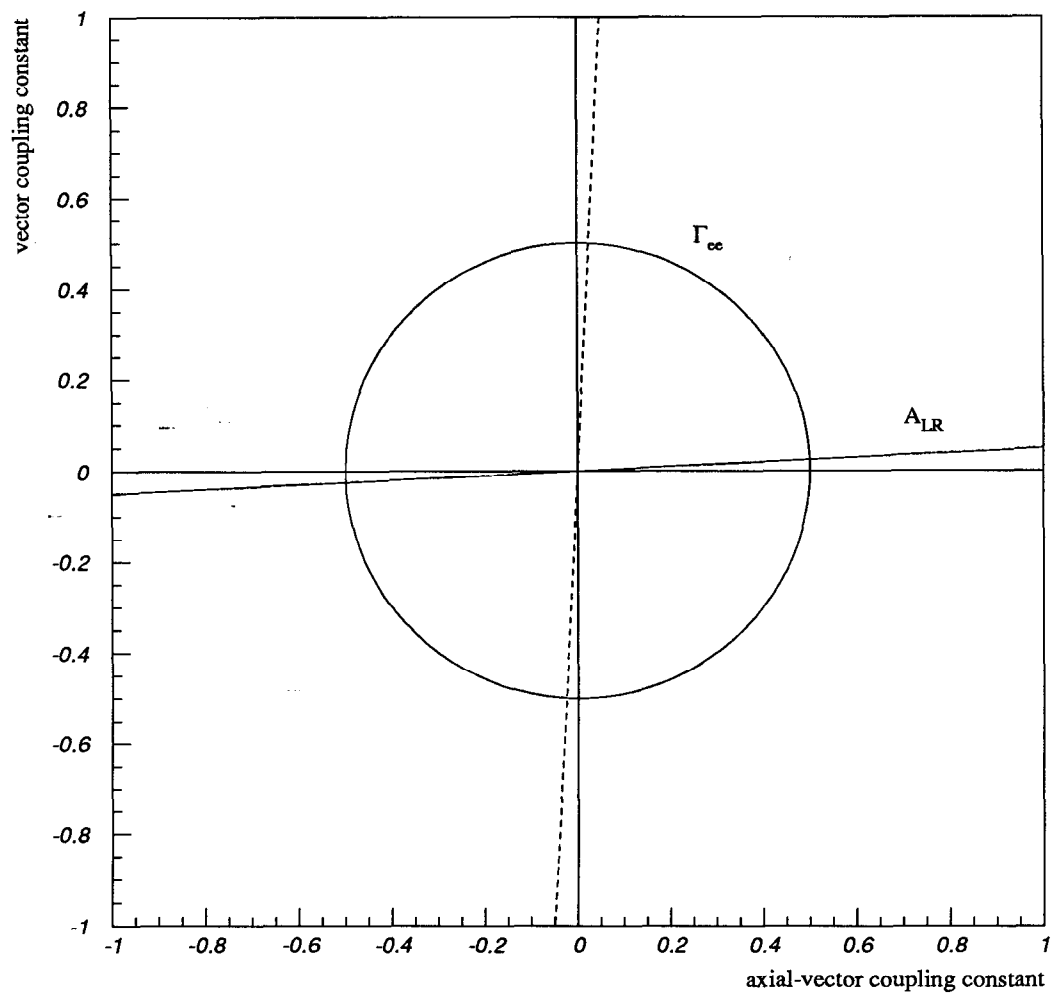


**Figure 1-6:**  $\Gamma_{ee}$  and  $A_{LR}$  in the vector – axial-vector plane. The electron partial width  $\Gamma_{ee}$  is shown as a circle and  $A_{LR}$  is shown as two lines. The solid line is the axial dominated solution for  $A_{LR}$

$$C_{SM} \equiv \frac{G_F M_Z^3}{6\sqrt{2}\pi}.$$

From Table 1.2,  $C_{SM} = 331.76 \pm 0.08$  MeV.

The overall sign ambiguity in eq(1.7) is resolved by  $\nu$  scattering experiments [9]. These demonstrate that the correct solution has both couplings negative.

## Chapter 2

# Bhabha Scattering at the $Z^0$

### 2.1 Lowest Order Bhabha Cross Section

The Bhabha scattering reaction ( $e^+e^- \rightarrow e^+e^-$ ) has, in addition to the annihilation graphs shown in Figure 1-1, exchange graphs. The four graphs are shown in Figure 2-1.

At the  $Z^0$  resonance, the leading terms in the cross section are the  $Z$  annihilation,  $\gamma$  exchange, and interference terms denoted by  $\sigma_{zszs}$ ,  $\sigma_{\gamma t \gamma t}$  and  $\sigma_{zs\gamma t}$  respectively:

$$\sigma = \sigma_{zszs} + \sigma_{\gamma t \gamma t} + \sigma_{zs\gamma t} + \text{small}, \quad (2.1)$$

where *small* refers to the non-leading terms in the cross section.

The relative strengths are determined by the angular acceptance of the detector and  $E_{cm}$ , with the interference term vanishing at the  $Z^0$  pole. The analysis presented here will be blind to the charge of the  $e^+$  or  $e^-$  since the event identification will

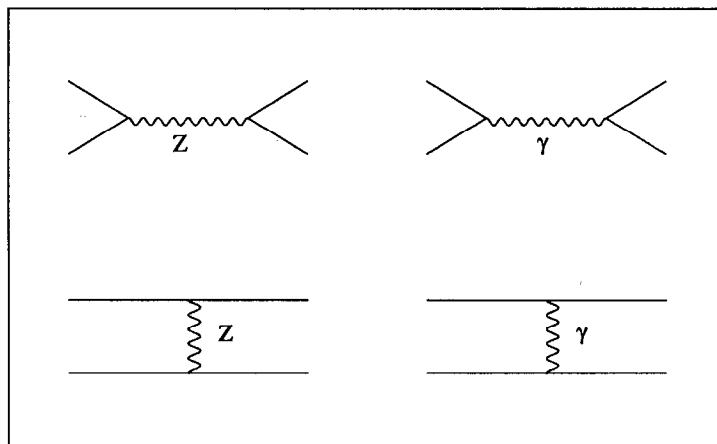


**Figure 2-1:** Feynman diagrams for Bhabha scattering to lowest order.

be done using only a calorimeter which does not have enough angular resolution to determine the charge sign orientation of the event<sup>1</sup>. For this reason, we will define the wide angle Bhabha cross section,  $\sigma_{ee}$ , to be the cross section into a symmetric polar angular range, where the polar angle,  $\theta_s$ , is the angle between the  $e^+$  or  $e^-$  and the beam line.

$$\sigma_{ee} = \int_{-\cos\theta_s}^{+\cos\theta_s} \frac{d\sigma}{d\cos\theta} d\cos\theta \quad (2.2)$$

where  $\frac{d\sigma}{d\cos\theta}$  is the polar angular distribution of the final state particles.

This definition is in contrast to the small angle Bhabha scattering cross section which is defined to be into a narrow angular range near the beam line (see section 5.3).

---

<sup>1</sup>Calorimeters in a magnetic field, with adequate angular resolution, can determine the charge sign orientation of the event by measuring the azimuthal sense of the magnetic field induced acolinearity of the two Bhabha showers.



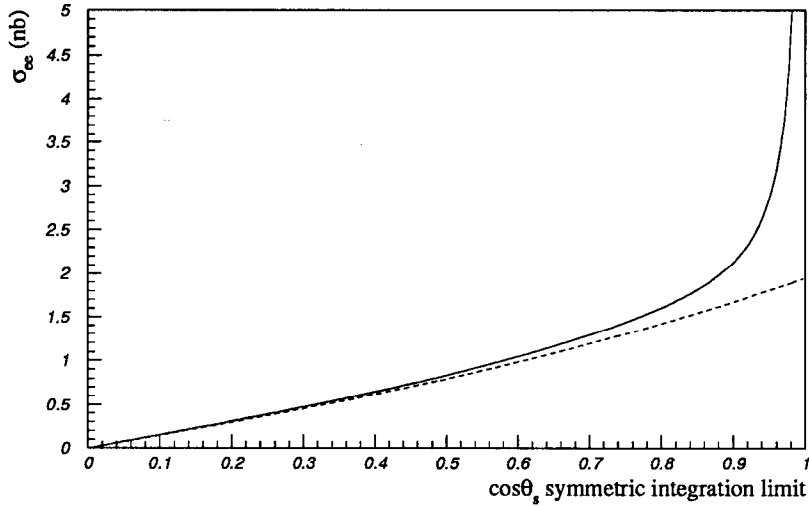


**Figure 2-2:** The wide angle Bhabha cross section vs.  $\cos \theta_s$ . The dashed curve is for annihilation only case, i.e.  $e^+e^- \rightarrow \mu^+\mu^-$ .

By evaluating the graphs in Figure 2-1 at the  $Z^0$  pole and performing the integral in eq. (2.2), we can determine wide angle Bhabha cross section (to lowest order),  $\sigma_{ee}$ , as a function of the symmetric integration limit,  $\cos \theta_s$ . This is shown in Figure 2-2. The dashed curve is the result for the pure annihilation case, i.e.  $e^+e^- \rightarrow \mu^+\mu^-$ .

Note that the cross section vanishes for the case where  $\cos \theta_s = 0$ . This is simply because the integration range in eq. (2.2) vanishes. The cross section is very similar to the pure annihilation case up to a  $\cos \theta_s$  of  $\sim 0.8$ , at which point the divergent  $\gamma_t\gamma_t$  term begins to dominate.

The annihilation term,  $\sigma_{z_s z_s}$ , can be written in terms of the decay width,  $\Gamma_{ee}$ .

$$\sigma_{z_s z_s} = \frac{12\pi\Gamma_{ee}^2}{M_Z^2\Gamma_Z^2} \cdot \left( \frac{\cos \theta_s + (\cos^3 \theta_s)/3}{4/3} \right) \quad (2.3)$$

Writing the annihilation term in this manner allows one to determine the partial width,  $\Gamma_{ee}$ , from the cross section measurement in a manner which is independent

of the Standard Model definition of  $\Gamma_{ee}$  (see section 1.5). In other words,  $\Gamma_{ee}$  is the physical width including, by definition, all corrections (except QED corrections which will be explicitly accounted for).

The interference term can also be written using  $\Gamma_{ee}$  instead of the Standard Model dependant parameters. The other dominant term,  $\sigma_{\gamma\ell\gamma\ell}$ , has no dependence on  $\Gamma_{ee}$ .

The small terms in eq. (2.1) which involve the  $Z^0$  cannot be written in terms of the physical width  $\Gamma_{ee}$  and therefore there will be some very small model dependence to the calculation which will be evaluated in section 2.3.

## 2.2 Sensitivity of $\sigma_{ee}$ to $\Gamma_{ee}$

One way to understand the leading terms and how they effect the measurement is to determine the sensitivity of  $\sigma_{ee}$  to  $\Gamma_{ee}$ . This is done by constructing the sensitivity function  $S(\Gamma_{ee})$ . Since the relative strengths of the leading terms are dependent on  $\cos\theta_s$  we will construct  $S(\Gamma_{ee})$  as a function of  $\cos\theta_s$ . The sensitivity function will tell us the statistical precision on our measurement of  $\Gamma_{ee}$ . The error on  $\Gamma_{ee}$  is given by

$$\Delta\Gamma_{ee} = \left( \frac{d\sigma_{ee}}{d\Gamma_{ee}} \right)^{-1} \Delta\sigma_{ee}. \quad (2.4)$$

The error in  $\sigma_{ee}$  is given by

$$\Delta\sigma_{ee} = \frac{\sigma_{ee}}{\sqrt{N}} = \sqrt{\frac{\sigma_{ee}}{\mathcal{L}}}, \quad (2.5)$$

where  $N$  is the number of wide angle Bhabha events accumulated and  $\mathcal{L}$  is the integrated luminosity accumulated.

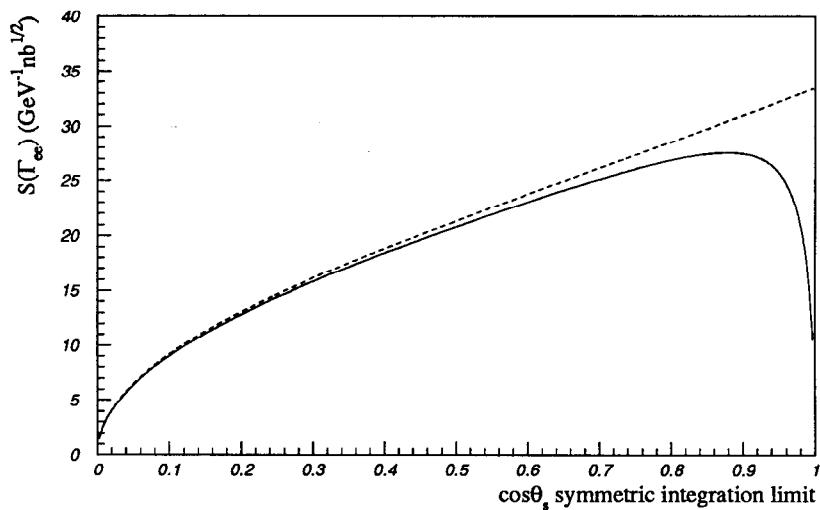


**Figure 2-3:** The Sensitivity function  $S(\Gamma_{ee})$  vs.  $\cos \theta_s$ . The dashed curve is for the case where there is no  $t$  –  $channel$  exchange

Combining these two equations we can write

$$\Delta \Gamma_{ee} = \frac{1}{\sqrt{\mathcal{L}}} \cdot \frac{1}{S(\Gamma_{ee})} \quad (2.6)$$

where

$$S(\Gamma_{ee}) \equiv \frac{1}{\sqrt{\sigma_{ee}}} \cdot \frac{d\sigma_{ee}}{d\Gamma_{ee}}. \quad (2.7)$$

We can see that the larger the sensitivity the smaller the error on  $\Gamma_{ee}$  for a fixed integrated luminosity.

We have evaluated  $S(\Gamma_{ee})$  in this way and plotted it vs.  $\cos \theta_s$  in Figure 2-3. The dashed curve is for the case where there is no  $t$  –  $channel$  exchange (note that the dashed line is *not* the sensitivity function for  $\Gamma_{\mu\mu}$  or  $\Gamma_{\tau\tau}$ ).

Note that the sensitivity increases as the integration limits are increased and then reaches a peak at  $\cos \theta_s$  of  $\sim 0.88$ . Beyond that the cross section is beginning to become dominated by the  $t$  - *channel* process which is not sensitive to  $\Gamma_{ee}$ . Figure 2-3 tells us that the maximum sensitivity for measuring  $\Gamma_{ee}$  is to integrate the cross section out to  $\cos \theta_s \sim 0.88$ , or about  $30^\circ$  from the beam line.

## 2.3 Model Independent Bhabha Approximation

A FORTRAN fitting routine called MIBA ("Model Independent Bhabha Approximation") [10] has been written which calculates the wide angle Bhabha cross section according to the procedure above. It is model independent in that the " $Z$ " part of the calculation is simply treated as a Breit-Wigner with a mass,  $M_Z$ , total width,  $\Gamma_Z$ , and electron width,  $\Gamma_{ee}$ . QED corrections are then applied to this procedure.

### QED Radiative Corrections

QED radiative corrections are applied to the lowest order Bhabha scattering process. The calculation includes complete  $O(\alpha)$  and leading-log  $O(\alpha^2)$  corrections. MIBA is quoted to have an accuracy of 0.5%. The vertex and loop corrections have been absorbed into the definition of  $\Gamma_{ee}$  (see eq. (2.3)).

### Inputs

The constant inputs to MIBA (for this analysis) are the recent precision results for the mass and total width of the  $Z^0$  [6] as well as  $\alpha$  and (for the non-leading terms)  $\sin^2 \theta_w$ . The experimental inputs are  $E_{cm}$ ,  $\cos \theta_s$  (MIBA allows asymmetric cuts for the case where the charge of the particle is known) the maximum acolinearity angle,  $\Theta_{acol}$ , between the  $e^-$  and the  $e^+$ , and the measured cross section,  $\sigma_{ee}$ .

If cross section measurements are made at several different energies around the  $Z^0$  resonance it is possible to simultaneously fit for  $\Gamma_{ee}$ ,  $M_Z$  and  $\Gamma_Z$ . However, the data taken in 1992 were only taken at one energy. Therefore,  $M_Z$  and  $\Gamma_Z$  must be supplied.  $\Gamma_{ee}$  is varied to produce a relation between the cross section and  $\Gamma_{ee}$ . The cross section measurement with its errors then determines the value for  $\Gamma_{ee}$ .

### Extracting $\Gamma_{ee}$

$\Gamma_{ee}$  is extracted by comparing the measured cross section,  $\sigma_{ee}$  to the curve of  $\sigma_{ee}$  vs.  $\Gamma_{ee}$  generated by MIBA. An example of this curve is given in Figure 2-4. The experimental inputs of  $E_{cm} = 91.28$  GeV,  $\cos \theta_s = 0.88$  and  $\Theta_{acol} < 20^\circ$  were chosen to illustrate the dependence.

Varying  $\sin^2 \theta_w$  by  $\pm 0.01$  (a large variation) changes  $\sigma_{ee}$  by  $\pm 0.02\%$ . This is a negligible change which verifies the assertion that the calculation is model independent. If the small terms in eq. (2.1) are completely ignored then the total cross section,  $\sigma_{ee}$  is at most 0.5% (and smaller for large  $\cos \theta_s$ ) less than the total cross section. This is equal to the quoted accuracy of MIBA.

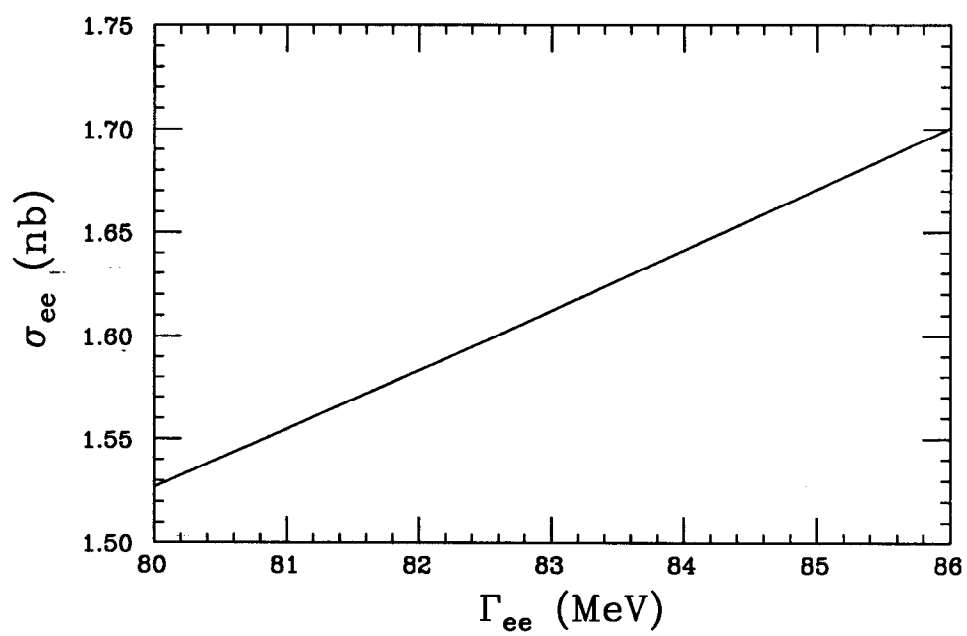


**Figure 2-4:** The theoretical dependance of  $\sigma_{ee}$  on  $\Gamma_{ee}$ . The cuts that define  $\sigma_{ee}$  are given in the text.

# Chapter 3

## The SLC and the SLD

This research was conducted at the Stanford Linear Accelerator Center (SLAC). SLAC is funded by the Department of Energy and managed by Stanford University. It is located on Stanford University land in Menlo Park California.

This chapter will describe the experimental facilities (machines and apparatus) which were used to make the measurement.

### 3.1 The SLAC Linear Collider

The SLAC Linear Collider (SLC) is the first accelerator to collide beams in a single pass manner and to produce  $Z^0$  events with  $e^+e^-$  collisions. It is also the first collider to produce  $Z^0$  events with a polarized electron beam. A brief description of the operation of the SLC with polarized electron beams is given below. A more detailed description is given in reference [11].

## The Collider

The polarized electron source produces two bunches of approximately  $6 \times 10^{10}$  electrons. The bunches are accelerated to 1.16 GeV and stored in the north damping ring of the SLC (see Figure 3-1). A positron bunch from the positron target is accelerated similarly and stored in the south damping ring. After damping, the positron and electron bunches are transported into the 3 km linear accelerator. The positron bunch and the first electron bunch is accelerated to 46.7 GeV. The trailing electron bunch is diverted onto a positron target after it reaches an energy of 30 GeV. The positrons that are collected are brought back to the front of the linear accelerator to participate in the next SLC cycle.

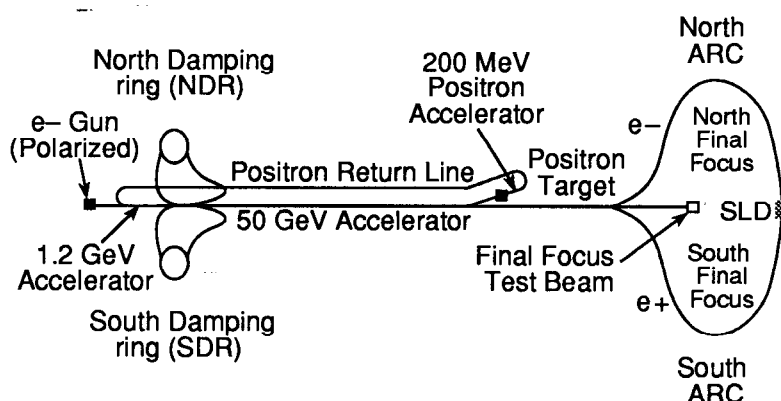


**Figure 3-1:** The layout of the SLAC Linear Collider.

After acceleration to 46.7 GeV the electron and positron bunches are oppositely directed into a pair of 1 km arcs which directs the bunches toward one another. Synchrotron radiation energy loss reduces the beam energy to 45.8 GeV. The beams are brought into a highly focussed collision and then pass into an extraction line and dumped. This operation is repeated at 120 Hz.

A system of solenoids is used to transport the spin of the polarized electron beam such that it has minimal losses in the north damping ring and such that its orienta-



tion is longitudinal at the SLC interaction point. The helicity of the electron beam is determined by the handedness of the circularly polarized laser beam pulse which produces the polarized electron beam. The laser beam handedness is randomly switched between left and right.

### Energy Spectrometer

The energies of the electron and positron bunches are measured by a pair of spectrometers in the extraction lines of the SLC [12]. The Wire Imaging Synchrotron Radiation Detector (WISRD) is a device which measures the deflection of the beam as it passes through a calibrated magnet. The deflection is measured via the synchrotron radiation which is emitted when the beam passes through two small bend magnets (orthogonal to the spectrometer magnet) which are there solely for the purpose of creating a synchrotron stripe (see Figure 3-2). The amount of deflection is inversely proportional to the energy of the beam, with the proportionality being the field integral of and distance to the calibrated spectrometer magnet. The energy of each beam pulse is measured for every beam crossing.

The center of mass energy,  $E_{cm}$ , for the 1992 run was 91.55 GeV. The systematic error on  $E_{cm}$  is 0.02 GeV [13].

### Polarimetry

The polarization of the electron beam is measured with a Compton scattering polarimeter [14]. The electron beam passes through a circularly polarized laser pulse at an interaction point 33 meters downstream of the SLC interaction point (see Figure 3-3). The polarimeter measures the Compton scattered electrons which are deflected from the beam line by an analyzing bend magnet. The polarimeter is a 9 channel Cherenkov detector which is sensitive to the position of the deflected  $e^-$ . The deflection distance is a measure of the electron energy. The energy (position) spectrum is

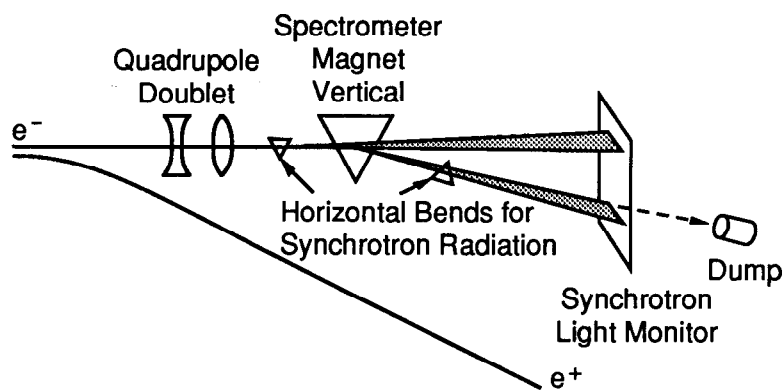


**Figure 3-2:** Schematic design of the extraction-line spectrometer.

measured for the case where the electron beam helicity and the laser beam helicity are aligned and anti-aligned. The asymmetry between these two distributions is a measure of the electron beam polarization (given the laser polarization). The mean  $e^-$  polarization for the 1992 run was 22.4%.

The helicity of the laser beam is randomly switched between left and right handed states to reduce systematic effects. There is also a proportional tube detector behind the Cherenkov detector which is used as a cross-check.

## 3.2 The SLC Large Detector

The SLC Large Detector (SLD) is a multi-purpose detector for studying  $e^+e^-$  colliding beam interactions [15]. It has a precision vertex detector, magnetic tracking, Cherenkov particle identification, liquid argon calorimetry followed by a iron streamer tube calorimeter, and a muon tracking system. A cutaway view of the SLD is shown in Figure 3-4.

Figure 3-5 shows a quadrant view of the full detector. The components will be

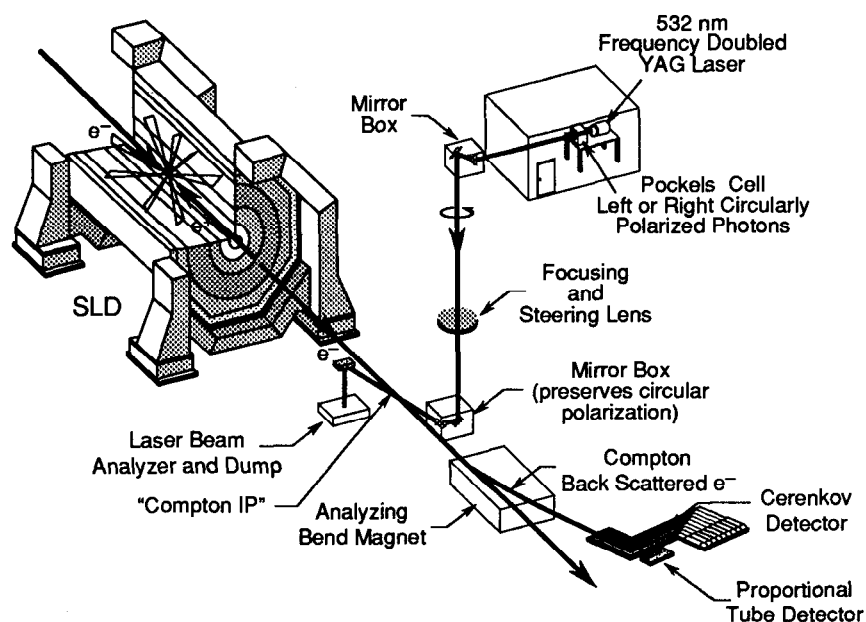


**Figure 3-3:** The Compton polarimeter system.

discussed in the following sections.

The measurement made here uses only the Liquid Argon Calorimeter (LAC) and the Silicon/Tungsten Luminosity Monitor/Small Angle Tagger (LMSAT). We will give a brief overview of the full detector and details of the LAC and LMSAT detectors.

### 3.2.1 Tracking

Charged particle tracking is accomplished by a precision vertex detector and a drift chamber which is composed of a barrel (central) drift chamber and two pairs of endcap drift chambers.

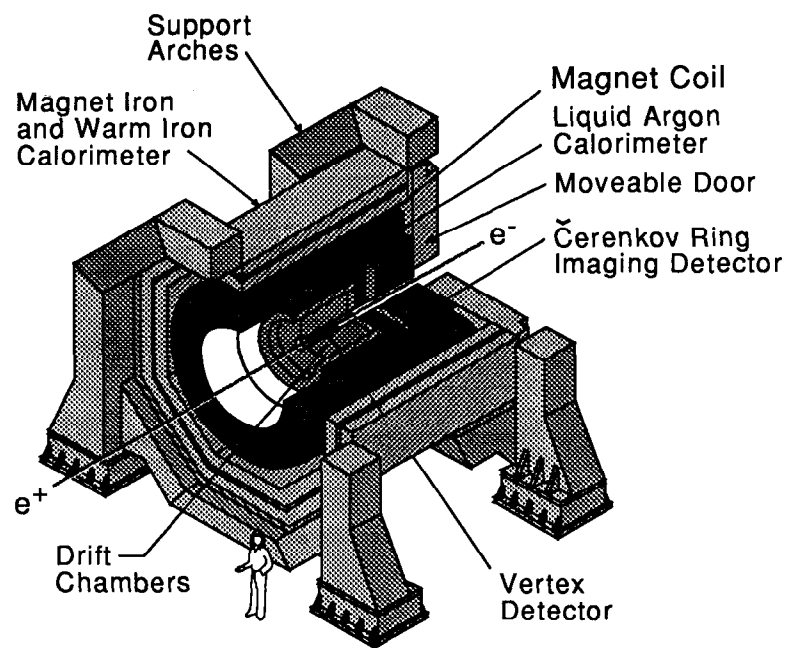


**Figure 3-4:** A cutaway view of the SLD.

### **The CCD Vertex Detector**

The CCD Vertex Detector (shown in Figure 3-6) is a silicon pixel detector which records the space points of charged particles [16]. It is located very close to the beam pipe of the SLC which allows it (when linked to the central drift chamber tracks) to precisely measure the impact parameter of charged tracks relative to the main interaction point of the event.

The Vertex Detector is comprised of 60 "ladders" of 8 CCDs each arranged in four concentric layers. Each CCD is composed of 25,000 pixels each 22 microns on a side. The position of the first layer is 29.5 mm from the beam line and the last layer is 41.5 mm.

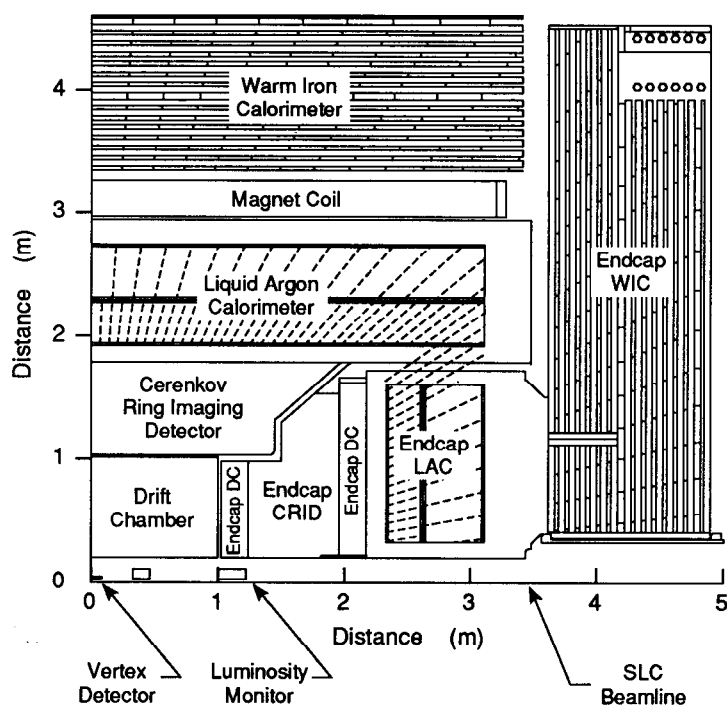
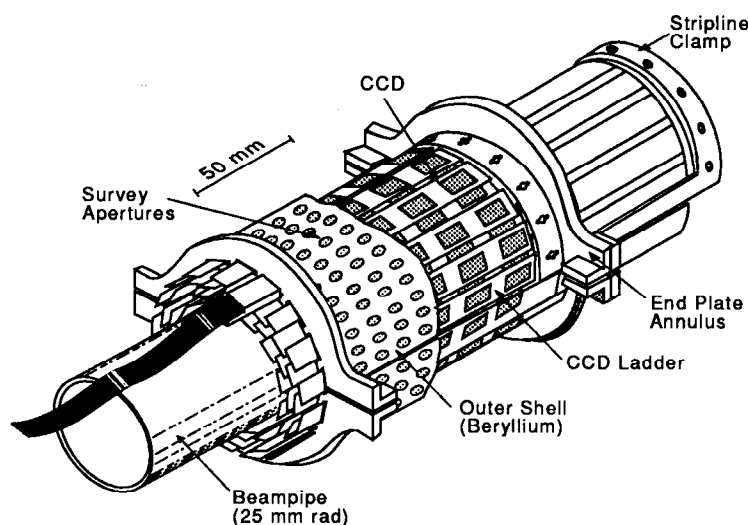


Figure 3-5: A quadrant view of the SLD.

### The Drift Chambers

The Central Drift Chamber (CDC) and the Endcap Drift Chambers (EDCs) are wire drift chambers which record the space points of charged particles as they pass through and ionize the gas in the chambers. The CDC [17] has 10 super-layers of 8 wires each for a total of 80 possible position measurements for a particle which exits through the outer cylinder of the chamber. The wire hits provide a measure of the radial position of the track. There are axial wires which are parallel to the beam line and stereo layers to provide a measurement of the position along the axis of the CDC. Charge division can also be used to determine this coordinate. The inner radius of the CDC is 20 cm and the outer radius is 100 cm. The length is 200 cm. The 0.6 Tesla magnetic field produced by the SLD solenoid enables the momentum of charged particles to be determined.



**Figure 3-6:** The CCD vertex detector.

The EDCs [18] provide tracking information for tracks which exit through the ends of the CDC. They are located 1.1 and 2.1 meters from the interaction point along the beam line on either side. Each of the four chambers is comprised of three super-layers with the orientation of the wires in the three layers being  $120^\circ$  to one another.

### 3.2.2 Particle Identification

Particle identification with the SLD is achieved via conventional techniques for electrons and photons (using tracking and calorimetry) and muons (using tracking and muon chambers). In addition, there is a detector which images the Cherenkov radiation of charged particles to achieve particle identification. This detector is known as the Cherenkov Ring Imaging Detector (CRID) [19].

## The CRID

Beyond the CDC and between the EDC pairs lay the barrel and endcap CRIDs. These instruments image the Cherenkov radiation that is emitted when a charged particle traverses the ( $C_5F_{12}$ ) gas and ( $C_6F_{14}$ ) liquid radiators of the device (if the speed of the charged particle is greater than light in the radiator). The imaging is accomplished with parabolic mirrors which focus the Cherenkov light cone to an ethane plane of 0.1% tetrakis(dimethylamino)-ethylene (TMAE). The image of the light is detected as a ring of photo-electrons in the TMAE. The photo-electrons are drifted (by an applied electric field) to single electron detectors at the end of the device (see Figure 3-7). The ring is reconstructed using the timing information that is recorded with each photo-electron.

The radius of the ring(s), when associated with a charged track and its momentum measurement is used to infer the identification of the charged track.

### 3.2.3 Calorimetry

The calorimetry of the SLD is a hybrid system composed of a Lead-liquid Argon Calorimeter (LAC) [20] and the Warm Iron Calorimeter (WIC) [21]. The LAC has an electromagnetic section and a hadronic section. The WIC is a hadron calorimeter which collects the (usually) small amount of energy that leaks out of the back of the LAC.

#### The LAC

The LAC barrel and endcaps are lead liquid-argon sampling calorimeters each with the same radiator structure. It has an electromagnetic (EM) section and a hadronic (HAD) section.

The structure of the EM section is alternating lead and liquid argon planes. The

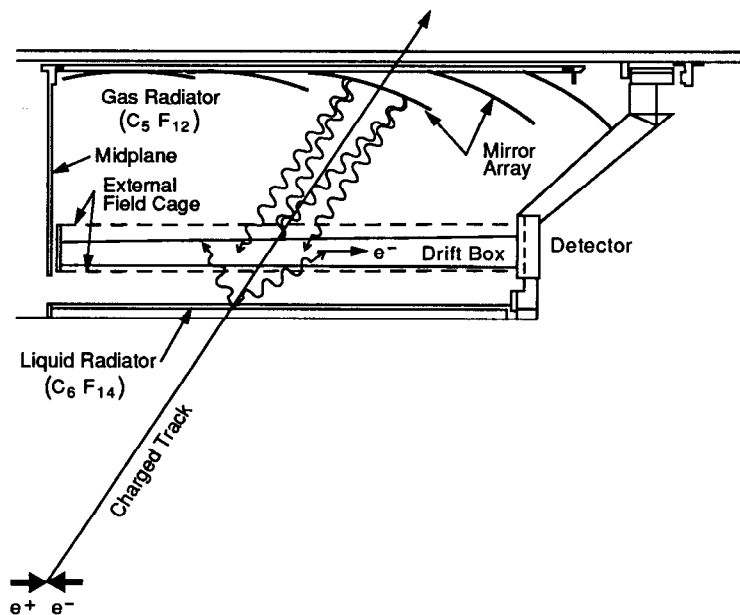


**Figure 3-7:** A view of a barrel CRID sector.

thickness of the lead is 2 mm and the liquid argon is 2.75 mm. This geometry has a sampling fraction of 18.4%. A cell is defined to be one lead plate and one layer of tiles. The tiles are the layer of lead which defines the azimuthal and polar tower structure. They are isolated from one another and are located projectively behind the tile of the previous cell. The lead plate is continuous across the whole EM module (a module is discussed later) and is separated with plastic spacers from the tile layer by 2.75 mm to make the liquid argon gap. Figure 3-8 shows a view of 2 cells of the calorimeter.

The EM section of the LAC is divided into  $\sim 33,000$  projective towers with  $\sim 26K$  in the barrel and  $7K$  in the endcaps. The barrel is divided into two radial sections, 192 azimuthal sections (each  $\sim 33$  mrad wide) and nearly 70 polar sections (each  $\sim 30$  mrad wide). The endcaps are also divided into 2 radial sections, 30 polar sections (15



on each end) and 192, 96, or 48 azimuthal sections depending on the polar position.<sup>1</sup>

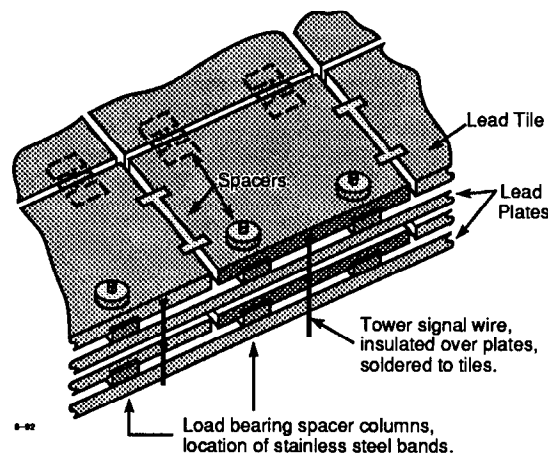


**Figure 3-8:** Two cells of the LAC.

The first radial section of the EM section, EM1, is made of 8 cells for a total of 6 radiation lengths ( $X_0$ ). The second EM section, EM2, is made of 20 cells for a total of 15  $X_0$ . The radial extent of the tower is accomplished by connecting successive tiles electrically to form a tower which also represents a single electronics channel.

The lead plates are held at ground and the tiles are held at a voltage of -2kV. Any ionization from the passage of a charged particle which occurs in the liquid argon in any of the layers of the tower is collected by the tiles to form the signal of the tower. There is no charge amplification in the liquid argon and a blocking capacitor is placed between the tower and the amplifier to filter out the -2kV dc signal.

The HAD section of the barrel LAC is similar to the EM section except that the number of polar and azimuthal divisions is half of what it is for the EM sections. This means that a single HAD tower lays behind 8 EM towers (2 radial  $\times$  2 azimuthal  $\times$

<sup>1</sup>the number of azimuthal divisions decreases as the polar position nears the beam line to keep the projective area of the tower from becoming too small.

2 polar). In addition, the lead is 6 mm thick instead of 2 mm as in the EM section. This means that the sampling fraction in the HAD section is 7.0%. Both of the HAD sections are composed of 13 cells each for a total of 2.0 interaction lengths ( $\lambda$ ) for the HAD sections of the LAC. The EM sections of the LAC total 0.84  $\lambda$ .

The lead plates and tiles are bundled into modules. Both EM sections form a module as do both HAD sections. Figure 3-9 shows a drawing of two EM modules and a HAD module. The modules have an aluminum base and top plate and are held together by thin steel straps. Endplates of the module have notches which properly place the module in the spool piece which holds all of the modules to form the LAC barrel.

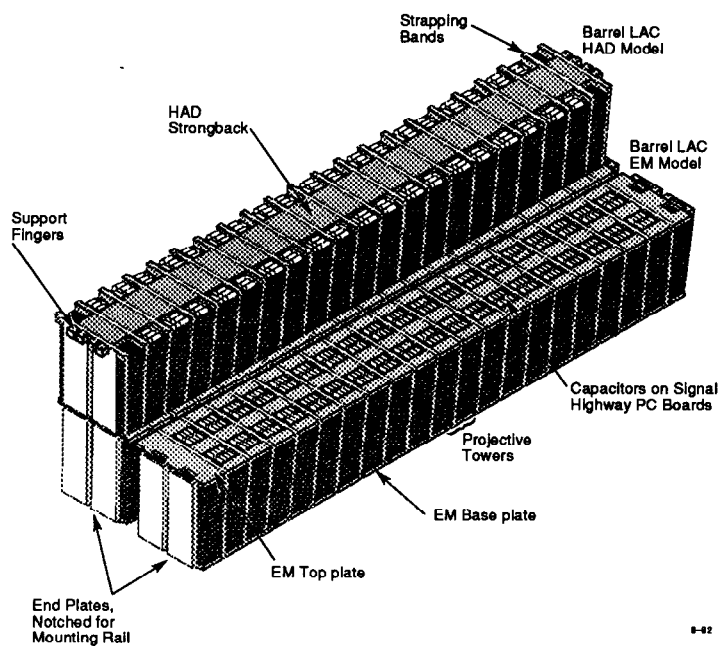


**Figure 3-9:** LAC barrel modules. Shown are two EM modules and one HAD module.

An exploded view of the LAC barrel assembly is shown in Figure 3-10 with all of

the cylinders which make the vacuum and argon vessels (the slings support the LAC barrel from the steel arches of the SLD). The inner argon cylinder is divided into three equal length bays. Washers separate these bays and grooves on the washers and end flanges guide the modules into place. There are 48 modules azimuthally for a total of 144 EM modules and 144 HAD modules.

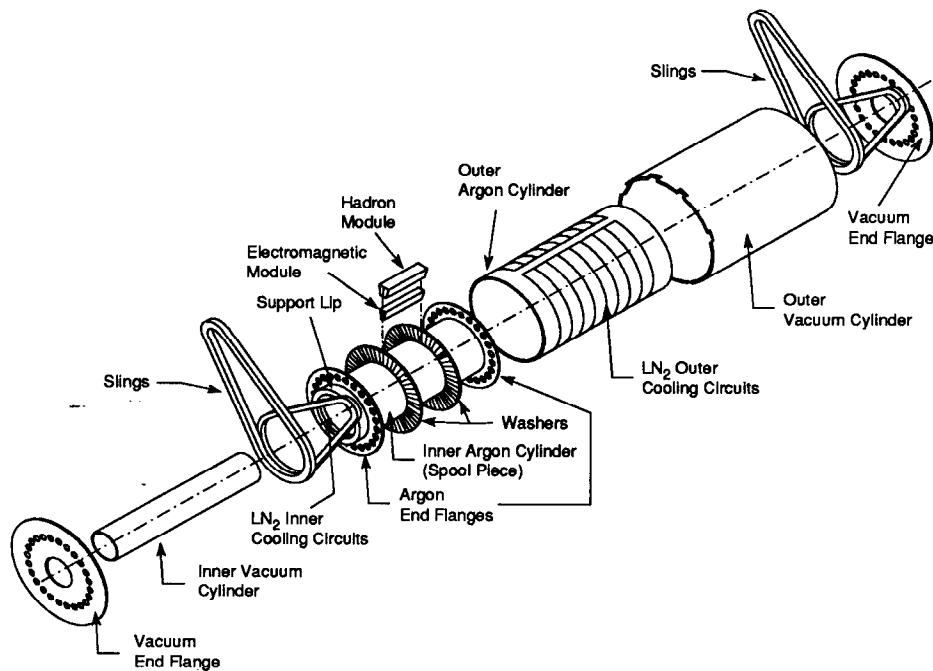


**Figure 3-10:** An assembly drawing of the LAC barrel showing the vacuum and argon vessels as well as the support slings.

The LAC endcaps are composed of modules which contain both the EM and HAD sections. There are 16 wedge shaped modules per endcap.

### The Warm Iron Calorimeter

The WIC is a steel – limited streamer tube, sampling calorimeter and muon tracker. There are 14 steel plates each 5 cm thick with 3.2 cm gaps between for the wire planes. The total thickness is 4.2 nuclear interaction lengths ( $\lambda$ ). The barrel WIC is the octagonal super-structure of the SLD that is shown in Figure 3-4. There are also two large endcaps on which are mounted the endcap LAC, CRID and EDC components.

The wire planes are composed of plastic streamer tubes which are bundled together to form planar chambers. The streamer signal is detected with external readout cathodes. One side of the chamber has projective copper pads which are aligned with the towers of the HAD section of the LAC. The other side of the chamber has copper strips which are 1 cm wide and run the length of the chamber to give a digital signal for muon tracking.

In the barrel the wires are oriented parallel to the beam line. In the endcaps the wires are perpendicular to the beam line. Two pad planes in the barrel are placed in front of the WIC to account for the absorption which occurs in the coil ( $0.6 \lambda$ ). The 16 planes of pad readout are ganged into two equal sections (inner and outer) to form the trailing sections of the SLD calorimeter system.

There are some strip planes in which the strip cathode runs transverse to the length of the chamber. These are incorporated into double wire plane chambers. These planes allow the measure of the streamer along the chamber length to help resolve tracking ambiguities. These transverse planes are located at the mid-point (radially) of the WIC and at the last layer.

In the endcaps, the wires of the inner part of the WIC are horizontal while in the outer part they are vertical.

### **3.2.4 Luminosity Monitor**

The luminosity monitor/small angle tagger (LMSAT) is a silicon/tungsten sampling calorimeter whose primary purpose is to record small angle Bhabha scattering events in order to measure the integrated luminosity [22]. The LMSAT is located 1 meter from the SLD interaction point (one on each side) and has an acceptance range of 28 to 65 mrad (see Figure 3-11). The inner edge of the LMSAT acceptance is defined by a tungsten snout which is 10 cm long and extends forward from its front face. The outer edge of the acceptance is defined by the inner edge of the Medium Angle Silicon

Calorimeter (MASiC). The MASiC fills the gap between the LAC and the LMSAT but has never been included in any trigger.

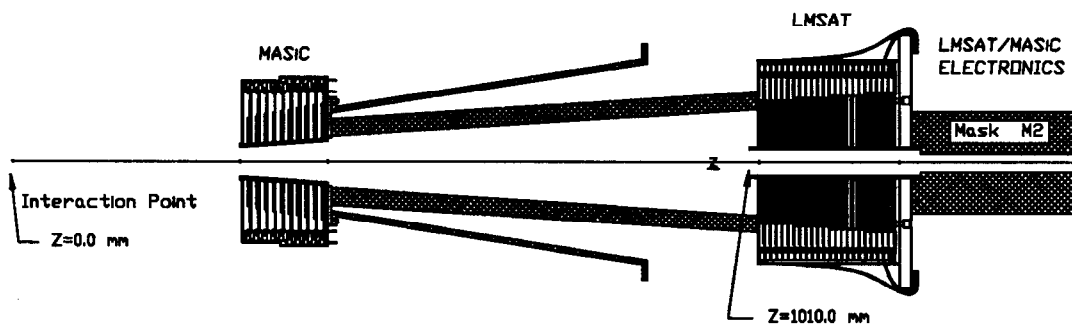


**Figure 3-11:** A side view showing the MASiC and LMSAT position with respect to the SLD interaction point.

The LMSAT is a sandwich of tungsten and silicon. There are 23 layer of alternating (90%)Tungsten/(10%)Cu-Ni and silicon layers. The sampling fraction of the device is 1.44% and has a design energy resolution of 3% at 50 GeV.

The LMSAT is divided into projective towers in much the same way as the LAC. A face on view of the LMSAT is shown in Figure 3-12. The first six layers of silicon are combined to form the first section (EM1,5.5  $X_0$ ) and the last 17 layers form the second section (EM2,15.6  $X_0$ ).

Each detector is composed of two modules which meet along a vertical plane through the beam line.

#### A $Z^0 \rightarrow \tau^+\tau^-\gamma$ Event

In order to demonstrate some of the SLD responses to various particles we present an event display of a low multiplicity  $Z^0$  decay. Figure 3-13 is an event display of a  $Z^0$  which decayed into a  $\tau$  pair and a  $\gamma$ . The  $\tau$  pair then decayed into an electron

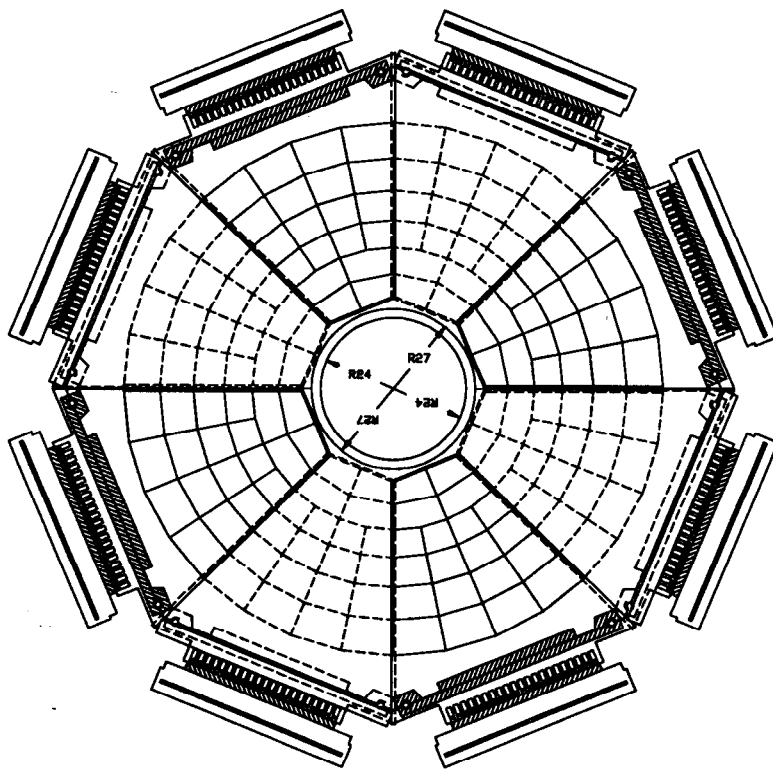


**Figure 3-12:** A face on view of the LMSAT showing the modular structure and the tower segmentation.

and a muon.

The muon is identified by the strip hits in the WIC which line up with the CDC track. The small squares in the calorimeter which line up with the track are the minimum ionizing tower signals in each of the four LAC layers and in the two WIC pad layers. The towers are displayed as squares whose areas are proportional to their energies.

The electron is identified by the tight shower in EM sections of the LAC (with no energy in the HAD sections) and which has a track pointing at it. The  $\gamma$  is the shower which has no track pointing at it.

Run 12956,	EVENT 2087
21-JUL-1992 13:35	
Source: Run Data	Pol: L
Trigger: Energy Hadron WAB	
Beam Crossing	2100643168

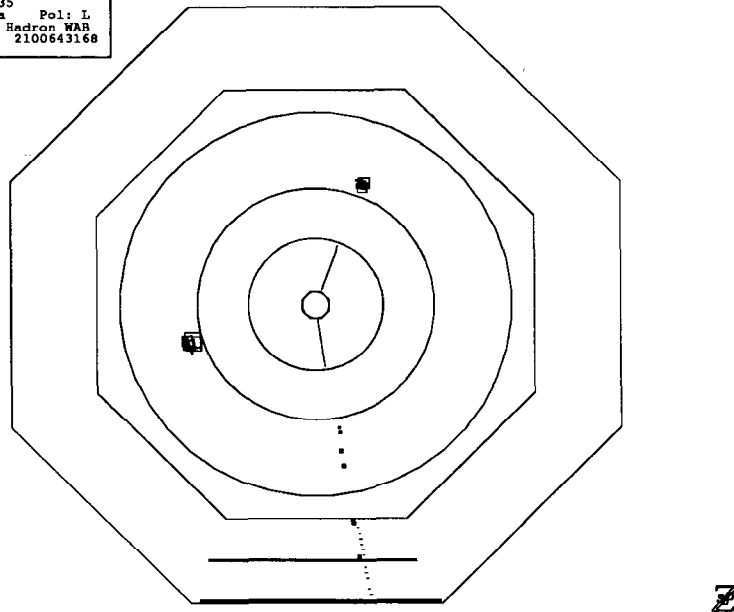


Figure 3-13: A display of a  $Z^0 \rightarrow \tau^+ \tau^- \gamma$  event.

### 3.3 Simulation

In order to determine the effects of the experimental apparatus which we have used to make our measurement, and to understand the effects of background, we need to simulate the physics processes and the detector in detail. This is achieved using event generators and detector simulation. In addition we will need to simulate the background conditions which were encountered during the run.

#### Event Generators

The physics processes which we expect to be occurring in the collision of  $e^-$  and  $e^+$  beams are mimicked with event generators. These generators produce a list of particles which represent the final state of the  $e^+e^-$  interaction.

Wide angle Bhabhas are simulated using the event generator BHLUMI version 3.11 [23]. It produces events with multiple hard and soft photons and is necessary to

calculate the efficiency for detecting and identifying wide angle Bhabha events.

The largest background process to wide angle Bhabha analysis is due to the purely QED process  $e^+e^- \rightarrow \gamma\gamma$ . It is simulated using the event generator RADCOR [24]. RADCOR contains virtual photon corrections, soft and hard bremsstrahlung to  $O(\alpha^3)$ .

The next largest background is due to  $e^+e^- \rightarrow \tau^+\tau^-$ . These events are simulated using the event generator KORALZ version 3.8 [25]. KORALZ has initial state radiative corrections to  $O(\alpha^2)$ , final state and electroweak radiative corrections to  $O(\alpha)$ .

The smallest of the backgrounds in consideration is due to multi-hadronic events. We simulate these events using the LUND event generator version 6.3 [26].

## GEANT

The SLD is simulated using the computer program GEANT version 3.11 [27]. GEANT uses the geometry and material description to simulate the environment which is encountered as a particle passes through the various detectors in the SLD. In addition, the response of the detector is simulated and digitized to simulate the format of the raw data. In this way, the data and Monte Carlo can be processed with identical reconstruction routines.

The LAC response is simulated using a fast shower parameterization which is based on GFLASH [28].

## Background Simulation

Backgrounds are simulated by overlaying real data background events with simulated event generator events. This is accomplished most easily by using the small angle Bhabha events. These events will contain nothing in the LAC except the ambient



backgrounds most of which is produced by the SLC (see section 4.1). In addition, the events represent a luminosity weighted sample of random beam crossings. This is important to correctly simulate the running conditions. The overlaying is accomplished by combining all the towers of the background events with the towers of the Monte Carlo event to produce the fully simulated event.

# Chapter 4

## Triggering and Event Selection

### 4.1 Backgrounds and Triggering Strategy

#### 4.1.1 SLC $\mu$ Background

Beam losses on components along the SLC arc orbit produce secondary particles. Among those produced are muons which can be trapped in the beam transport and accompany the beam to the SLC interaction point. Beam transport components also cause the muons to leave the orbit of the main bunch of electrons (or positrons as the case may be) and travel at a larger radius down the final straight section toward the SLD. These muons then pass through the SLD parallel to the beam line depositing energy in the LAC. Figure 4-1 shows an event display of hits in the LAC barrel and endcaps in a luminosity Bhabha event (the luminosity monitor is not shown) The streaks of towers from the muons are clearly evident in the LAC barrel. The short streaks at each end of the LAC are muons passing through the end caps.

In order to illustrate the problem with the beam associated muons, the small angle Bhabha events that are recorded in the luminosity monitor are used. These

Run 11341,	EVENT 714
9-MAY-1992 05:01	
Source: Run Data	Pol: L
Trigger: Bhabha	
Beam Crossing	341212

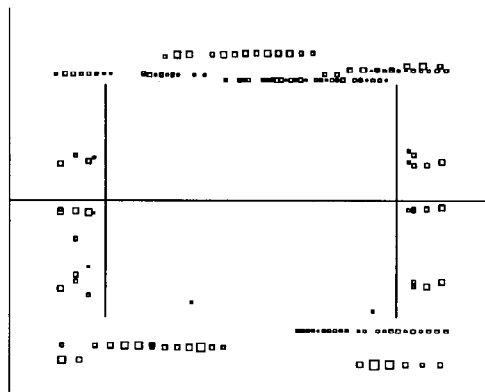


**Figure 4-1:** Display of LAC hits for a luminosity Bhabha event.  
Top view of the LAC for an event which was triggered by a small angle Bhabha event. The SLC  $\mu$  streaks are evident in the barrel. Individual LAC tower hits are displayed with the size of the box proportional to the energy.

events provide a luminosity weighted sample of random beam crossings which record the beam backgrounds in the LAC. A pattern recognition algorithm (see Appendix A) can flag clusters that are induced by the SLC muons. Figure 4-2 shows the multiplicity of found muons in the barrel LAC for small angle Bhabha events (It is important to note that the pattern recognition works less efficiently for high muon multiplicity events because the clustering will group the muon clusters together and will thus prevent recognition). The distribution tells us that 95 percent of the beam crossings have 2 or fewer muons in the barrel LAC. This is not a problem for event analysis as they only deposit a few GeV and in addition can be removed relatively easily. The distribution also tells us that there is roughly a 1 Hz rate for five or more muons to traverse the LAC barrel. This causes a problem for triggering since five or more muons deposit on average more than 20 GeV (with large fluctuations) in the Barrel LAC.

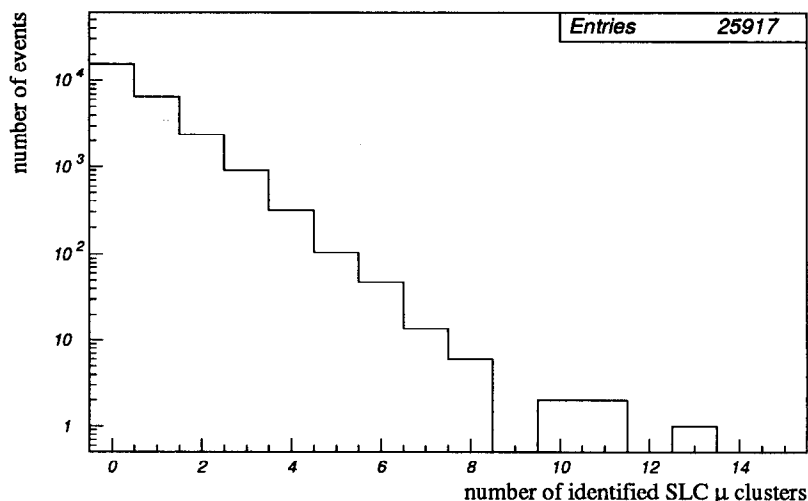


**Figure 4-2:** The number of identified  $\mu$  induced clusters found in the LAC barrel per small angle Bhabha event.

### 4.1.2 Trigger Algorithm

The strategy for suppressing the muons while still maintaining good efficiency for hadronic and wide angle Bhabha events is revealed by studying the tower ADC spectra for identified SLC muons. Figure 4-3 shows the ADC spectra for muons in the EM section and HAD section of the LAC. In order to make the trigger less sensitive to the muons, a high threshold is applied to each tower which contributes to the trigger sums (the trigger sums will be defined later). This effectively blinds the trigger to the muons. The high thresholds are 60 ADC in the EM sections and 120 ADC in the HAD sections [29] and are shown in Figure 4-3.

The peaks of the EM and HAD distributions are roughly at the same ADC value. However, the high threshold is set higher in the HAD section because the cross-sectional area of the HAD sections of the LAC is more than twice that of the EM sections. Therefore more muons from the SLC are detected by the HAD sections. In addition, only about 30% of the raw energy that is deposited into the LAC from the hadronic decay of a  $Z^0$  is detected in the HAD sections. Therefore it is advantageous

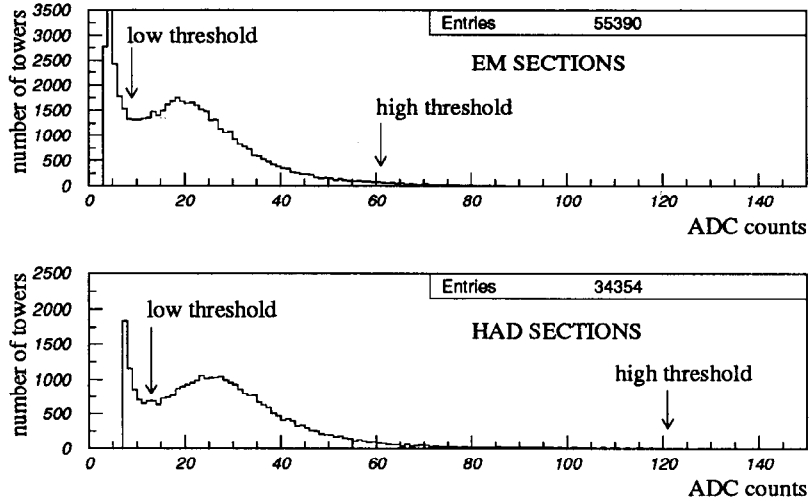


**Figure 4-3:** ADC spectra for  $\mu$  induced clusters in the LAC barrel. The ADC spectra for hits in clusters which were induced by a  $\mu$  in the LAC barrel. The upper plot is for hits in the EM sections of the LAC and the lower plot is for the HAD sections.

to set the thresholds higher in the HAD section.

The trigger sums are also accumulated for a low set of thresholds which are below the main peak but above the noise peak. These sums are sensitive to the SLC muon background and useful for the SLC operators to monitor while they are tuning the beams. In addition, the low threshold (8 ADC in the EM and 12 in the HAD) trigger sums are useful for vetoing during data acquisition and in offline event selection.

The trigger separately accumulates the sum of the energy in all towers above the high or low threshold in the EM and HAD section, for the barrel and endcap and for north and south side of the detector separately. Minimum ionizing energy loss in the LAC is  $\sim 2.8 \text{ ADC/MeV}$  in the EM and  $\sim 7.5 \text{ ADC/MeV}$  in the HAD section. The scales for the trigger were set higher to account for the invisible energy in electromagnetic and hadronic showers. The conversion from ADC to GeV in the trigger is 0.524 GeV per 128 ADC ( $\sim 4.1 \text{ ADC/MeV}$ ) in the EM section and 1.384 GeV per 128 ADC ( $\sim 10.8 \text{ ADC/MeV}$ ) in the HAD section. Wide angle  $e^+e^-$  events

would record  $\sim 100$  GeV on this scale. Hadronic events record less due to the non-compensating response of the LAC (see later section). The number of towers which contribute to these energy sums is also determined. These sums are used for the trigger decision. The trigger information is stored on tape along with any event which has satisfied the trigger.

It is convenient to define several of the sums in order to continue the discussion of the LAC trigger. The useful sums are:

**EH** is the sum of the energy in all towers above the high threshold.

**EL** is the sum of the energy in all towers above the low threshold.

**NL** is the number of towers above the low threshold.

**NEMH** is the number of towers in the EM section above the high threshold.

The ENERGY trigger required that EH be greater than 8 GeV with a veto which requires that NL be less than 1000 towers. If this requirement was satisfied then the entire calorimeter system of the SLD was read out (provided that the system was ready to be read out). Other triggers operating may also have been satisfied and would have requested that the entire SLD detector systems be read out. During the 1992 polarized run the SLD recorded to tape roughly 1 million ENERGY triggers.

## 4.2 PASS 1 Selection

In order to obtain an enriched sample of hadronic and wide angle Bhabha events, the events which have been recorded to tape are required to satisfy a PASS 1 filter [30]. The PASS 1 filter is based on the trigger sums which are determined online and recorded with the event. No processing of the data is required. The PASS 1 requirements are the following:

- $\text{NEMHI} \geq 10$  towers
- $\text{EHI} > 15 \text{ GeV}$
- $\text{ELO} < 140 \text{ GeV}$
- $\text{ELO} < \frac{2}{3} \text{EHI} + 70 \text{ GeV}$

The "ELO" requirements are in place to insure that the event hasn't satisfied the other requirements through the large deposition of beam background noise. There is a small chance that there is a real  $e^+e^-$  scattering interaction recorded in these events. This is calculated in the section on efficiency in chapter 5.

After the PASS 1 requirements are applied there are roughly 18 thousand events remaining. Figure 4-4 shows a scatter plot of EHI vs. ELO for the PASS 1 events. The three energy cuts are shown on the plot (solid). By definition no points can lie above the dashed line. The hadronic events can be seen as the oval distribution of points. Wide angle Bhabhas can be seen on the left edge of the distribution roughly near the center of the plot.

The hadronic events record  $\sim 60 \text{ GeV}$  in the ELO trigger variable and the wide angle Bhabha events record  $\sim 100 \text{ GeV}$ . This is because the response of the LAC to a hadronic event is less than for an  $e^+e^-$  event. This will be discussed in more detail in the next section. In addition one can see that hadronic events only record  $\sim 40 \text{ GeV}$  in the EHI trigger quantity. This is because a significant amount of energy in a hadronic event is deposited in towers which are below the HI tower trigger thresholds. The  $e^+e^-$  events record almost as much energy in the EHI trigger variable as in the ELO variable (therefore they lay close to the dotted line). This is because most of the energy from an  $e^+e^-$  event is deposited in towers above the HI trigger thresholds.

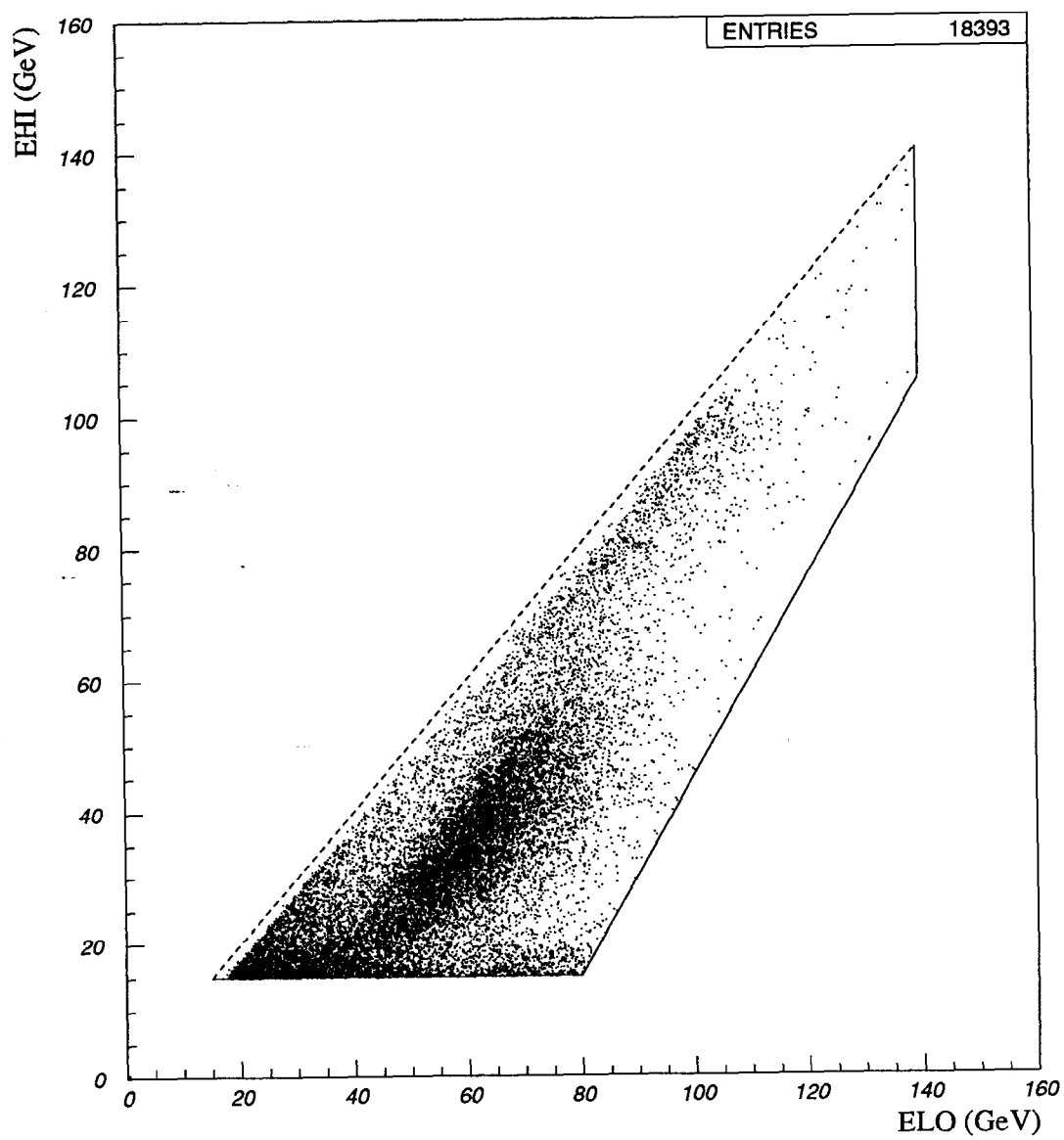


**Figure 4-4: PASS 1 Events.**  
The Trigger quantities EHI vs. ELO for all PASS 1 events.



## 4.3 Reconstruction and Energy Scale

### 4.3.1 Clustering

The events which satisfy the PASS 1 requirements are processed through the calorimetry reconstruction. All LAC towers are subject to a reconstruction threshold of 7 ADC for the EM sections and 9 ADC for the HAD sections<sup>1</sup>. The WIC pads are not included in this analysis. The reconstruction produces *clusters* from the hits. The clusters are a grouping of tower hits that are associated spatially. The first stage of clustering is to group all hits that are contiguous. These are called coarse clusters. The second stage is a refinement stage which takes the coarse clusters and looks for minima in the energy distribution and separates them if it appears as though the deposition is the result of more than one incident particle. These clusters are known as refined clusters.

The energy weighted mean position in  $\phi$  and  $\cos \theta$  is computed from the hits. The clusters are then vectors, which we will denote by  $\vec{k}$ . They can be thought of as momentum vectors for massless particles.

### 4.3.2 Energy Scale

The ADC count that is associated with each tower is converted into an energy on what is known as the minimum ionizing scale. The conversion assumes that the charge that is collected has arisen from a minimum ionizing particle that lost energy in the lead and argon. The sampling fraction is applied so that the average total energy loss in the LAC is determined. This energy will be referred to as *raw* energy since energy which does not show up as ionization in the liquid Argon is not taken into account.

In hadronic or electromagnetic showers, there is energy which does not show up

---

<sup>1</sup>The readout threshold is 2(3) ADC in EM1(2) and 6 ADC in the both HAD sections.

as ionization. In the case of hadronic showers, energy can be lost due to neutrons carrying away energy undetected and also due to nuclear binding energy in the hadronic collisions of the shower. Neutrinos from  $\pi$  decay can also account for some of the undetected energy. Electromagnetic showers produce a large number low energy electrons, positrons and photons. Because of the very soft spectrum of shower particles and the lower efficiency for converting low energy particles to ionization, some of the energy is undetected.

All these effects reduce the output of the calorimeter relative to the minimum ionizing expectation. The reduced response is called the  $\pi/\mu$  or  $e/\mu$  ratio for hadronic and electromagnetic showers respectively. In general,  $\pi/\mu$  and  $e/\mu$  have different values<sup>2</sup>. This means that the calorimeter will respond with a different integrated signal for hadrons and electromagnetic (electrons and photons) particles. The degree to which  $\pi/\mu$  and  $e/\mu$  do not match is called the  $e/\pi$  ratio. This is the ratio of the response of an electromagnetic particle to the response of a hadronic particle of the same energy. The  $e/\pi$  ratio for the LAC is approximately 1.7 based on an analysis of the 1992 data [31]. This means that an electron, for example, with an energy of 45.7 GeV will produce a response which is 1.7 times the response of a pion of the same energy. There will not be any correction for the  $e/\mu$  or  $\pi/\mu$ . All energies will remain *raw*. For the purposes of identifying  $e^+e^-$  events, a large  $e/\pi$  proves to be an advantageous characteristic as  $e^+e^-$  events will tend to be separated from the tau and hadronic events just by the raw response alone.

### 4.3.3 $\pi^0$ Mass Reconstruction

One way to determine the electromagnetic scale ( $e/\mu$ ) is to search for neutral  $\pi$  mesons in the data [31]. Determining the mass of the  $\pi^0$  on the raw energy scale will allow us to predict the response of the LAC to wide angle Bhabha events.

---

<sup>2</sup>A calorimeter which has  $\pi/\mu$  equal to  $e/\mu$  is called a compensating calorimeter

Photon ( $\gamma$ ) candidate clusters<sup>3</sup> are chosen via the following cuts:

- $|\cos \theta| < 0.6$
- $4 \leq N_{towers} \leq 100$
- $E_{EM} > 0.5$  raw GeV
- $f_{EM} > 0.93$
- $f_3 > 0.8$

where  $\theta$  is the polar angle of the cluster,  $N_{towers}$  is the number of towers in the cluster,  $E_{EM}$  is the raw energy in the EM section of the cluster,  $f_{EM}$  is the fraction of energy in the EM section of the cluster, and  $f_3$  is the fraction of energy in the three most energetic towers in the cluster.

The event is required to have less than 11 such candidates to reduce the combinatoric background. All  $\gamma\gamma$  pairs have the following cuts applied:

- $0.5 < \cos \theta_{\gamma\gamma} < 0.9975$
- $E_{\gamma\gamma} > 1.75$  raw GeV

where  $\theta_{\gamma\gamma}$  is the opening angle between the  $\gamma$  candidates, and  $E_{\gamma\gamma}$  is the energy of the pair.

Figure 4-5 is a plot of the invariant mass,  $m_{\gamma\gamma}$ , of pairs of  $\gamma$  candidates which satisfy the above requirements. The distribution is fit to a gaussian for the  $\pi^0$  peak and a third order polynomial for the background. The fit gives a  $\pi^0$  mass of  $105.3 \pm 1.5$  raw MeV. By varying the selection cuts systematic errors are determined to be approximately the same size as the fit error.

---

<sup>3</sup>Because the photon energies are low, the reconstruction ADC threshold was reduced to the readout threshold for this analysis

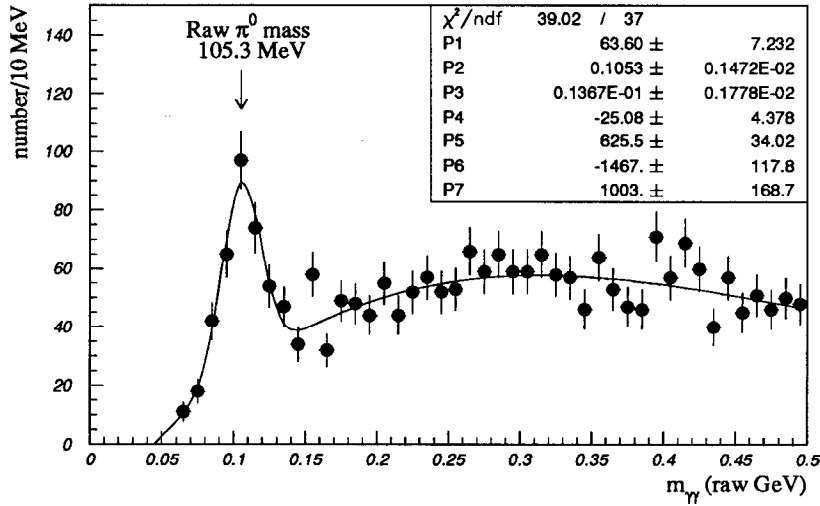


**Figure 4-5:**  $\gamma\gamma$  invariant mass distribution.  
The fit is to a gaussian and a third order polynomial

Given that the *real*  $\pi^0$  mass is 134.97 MeV [5] we determine the  $e/\mu$  for the LAC to be  $0.78 \pm 0.02$ . It should be noted that the minimum ionizing scale has not been determined precisely and therefore the  $e/\mu$  quoted has an additional undetermined error. However, the prediction for the response to wide angle Bhabhas is independent of the minimum ionizing scale error. We therefore expect that the raw energy response of the LAC to a wide angle Bhabha event will be  $(91.55\text{GeV}) \times (0.78 \pm 0.02) = 71.4 \pm 1.8$  raw GeV.

## 4.4 LAC Response to Bhabha and Hadronic events

In order to motivate some of the cuts which are applied in the section on wide angle Bhabha event selection (next section), a loose selection is made to observe the response of the LAC to the events (hadronic or Bhabha) recorded.

#### 4.4.1 Selection

All PASS 1 events are reconstructed. Each event is composed of a list of clusters. All clusters are examined by a pattern recognition routine which looks to see if the arrangement of hits is consistent with that of a cluster induced by an SLC muon (see Appendix A). SLC muon induced clusters are ignored as well as those clusters which have no energy in the EM sections and those clusters which fail a minimum raw energy cut of 100 MeV. The cluster multiplicity,  $N_{cl}$ , is the number of clusters in the event which satisfy these requirements.

The event is then analyzed and the following event quantities are evaluated:

$$E_{raw} = \sum_{i=1}^{N_{cl}} |\vec{k}|$$
$$I_{mb} = \left| \sum_{i=1}^{N_{cl}} \vec{k} \right| / E_{raw}.$$

$E_{raw}$  is the total raw energy in the event and  $I_{mb}$  is the imbalance of the event. In addition, the cosine of the polar angle of the most energetic cluster in the event,  $\theta_1$  is determined.  $\theta_1$  is a rough indicator of the polar angle of the decay axis for hadronic events and is a good indicator for wide angle Bhabha events.

#### 4.4.2 Polar Angle Features of the LAC Response

Figure 4-6 shows the distribution of  $I_{mb}$  for all PASS 1 events. Hadronic and Bhabha events will have low  $I_{mb}$ . The events with a large imbalance are events which were triggered due to beam background or electronics noise. A cut on  $I_{mb}$  of 0.6 is applied and shown in the figure.

Figure 4-7 shows a plot of  $E_{raw}$  vs.  $|\cos \theta_1|$  for all PASS 1 events which satisfy

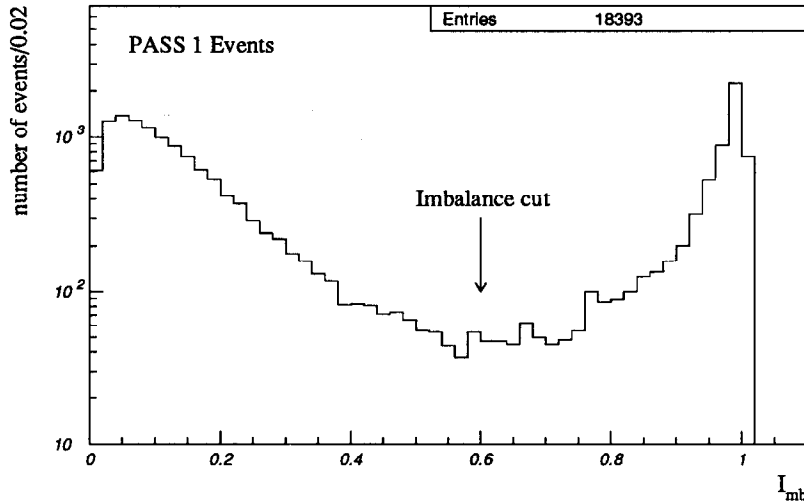


**Figure 4-6:**  $I_{mb}$  for all PASS 1 Events.  
The  $I_{mb}$  distribution for all events which satisfy the PASS 1 selection criteria.

the  $I_{mb}$  cut.

The hadronic events in the sample are represented by the large band running across the plot at an energy of  $\sim 40$  GeV. The wide angle Bhabhas can be seen as a thinner band at an energy of  $\sim 70$  GeV (as expected from the  $\pi^0$  mass analysis). Wide angle Bhabha clusters will tend to have their calculated position near the center of a tower because the showers are narrow and put most of their energy in one tower. This is why the plot shows short vertical bands at the expected Bhabha energy. They are essentially being plotted to the nearest tower center.

Note that the response of the LAC to wide angle Bhabhas and hadronic events changes at a  $|\cos \theta_1|$  of  $\sim 0.6$ . This has been shown to be due to material in front of the LAC from the inner detectors [32]. The response can be seen to increase again in the endcap region but with a much broader distribution in the case of the wide angle Bhabhas (whose yield can be seen to increase as expected). This is also attributed to material in front of the LAC endcap.

Note also the behavior near a  $\cos \theta_1$  of 0.45. The band at that location is showing

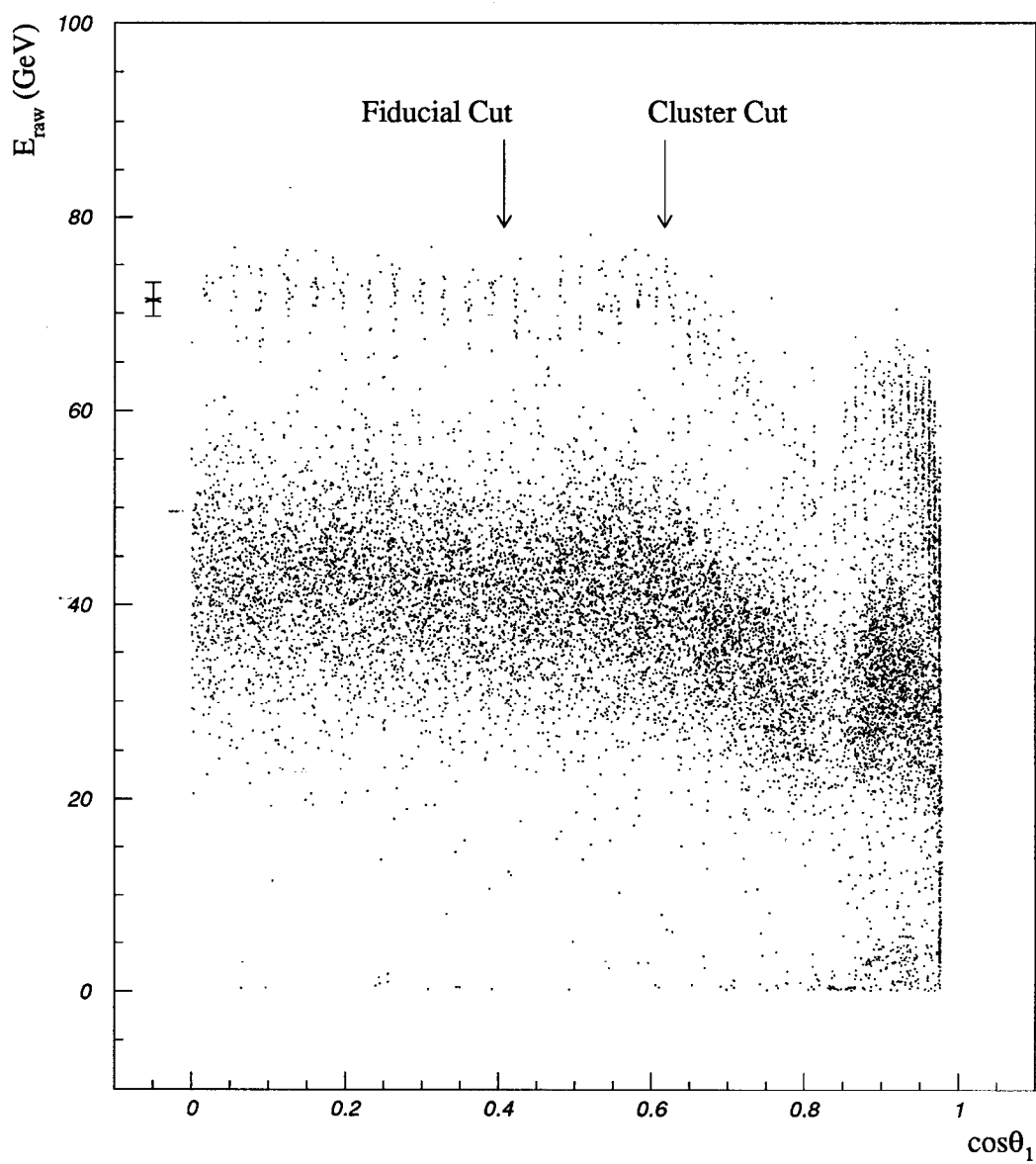


**Figure 4-7:** A scatter plot of  $E_{\text{Raw}}$  vs.  $|\cos\theta_1|$  for *balanced* events ( $I_{mb} < 0.6$ ). The cut markers are discussed in the text. The data point with error bars on the left margin of the plot is the expected mean response of the LAC to wide angle Bhabha events.

a poor response. This is the location of the washer(see Figure 3-10). In this region the towers are not complete and therefore do not detect the full response of the shower.

At the time of writing, the behaviors exhibited in Figure 4-7 were not properly reproduced by the Monte Carlo. Recent work on the Monte Carlo has improved the agreement with the data. However, this work is still in progress. Therefore, we take a conservative approach to the wide angle Bhabha analysis.

In order to avoid biases due to incorrect simulation, a cluster cut is applied to each cluster that is considered in the event analysis (shown in Figure 4-7 as cluster cut). This effectively creates a detector which is simply a barrel (shorter than the LAC barrel) that has uniform response along its length. In addition, the event will be required to have its two most energetic clusters to lie within the region of the LAC bounded by the washers (shown in Figure 4-7 as fiducial cut). This creates a *fiducial region* which is very uniform and easily simulated. Placing the fiducial cut inside the cluster cut is also necessary to insure that most of a hadronic event is contained within the cluster cut region and can be recognized as a high multiplicity event and rejected. These cuts will be reviewed in the next section.

## 4.5 Selecting Wide Angle Bhabha Events

We begin with all reconstructed PASS 1 events. The events are required to fall within a fiducial region of the LAC and then pass a set cuts designed to efficiently select wide angle Bhabha events while eliminating background.

### 4.5.1 Fiducial Definition

At this point it is necessary to *define* the sample which is to be studied. We will define a *fiducial* event to be one in which the two highest energy clusters have the



following properties:

- $|\cos \theta| < 0.407$
- $\Theta_{acol} < 20^\circ$

The  $|\cos \theta|$  cut places both showers of an  $e^+e^-$  event in the central bay of the LAC (between the washers). This is the fiducial cut shown in Figure 4-7.  $\Theta_{acol}$  is the acolinearity angle between the clusters. These cuts do not have an efficiency associated with them. This is because the fiducial cuts represent the definition of events that are to be compared to theory (this is true of any Bhabha analysis).

For the purposes of efficiency studies, Monte Carlo  $e^+e^-$  events will be identified at the generator level (before simulation of detector response) as a fiducial event. These will form the denominator in the efficiency calculation since they represent the process which is being considered. In other words, a sample of fiducial Monte Carlo  $e^+e^-$  events will be generated and passed through the simulation and selection cuts. What remains divided by the number of input events will be the overall efficiency.

#### 4.5.2 Cluster Selection

In order to select wide angle Bhabha events in the LAC, *good clusters* are required to have the following properties:

- $E_{EM} > 0.0$  GeV
- $E_{tot} > 0.25$  GeV
- $|\cos \theta| < 0.617$
- not flagged as an SLC  $\mu$

Where  $E_{EM}$  is the raw energy in the EM section of the cluster and  $E_{tot}$  is the energy in all LAC layers of the cluster. The  $|\cos \theta|$  cut is the cluster cut which is shown in Figure 4-7

### 4.5.3 Event Selection

Finally, the *event cuts* require the following:

- $N_{good} \leq 5$
- $E_{totEM} > 55 \text{ GeV}$

Where  $E_{totEM}$  is the total raw energy in the EM section of the LAC summing over all good clusters.

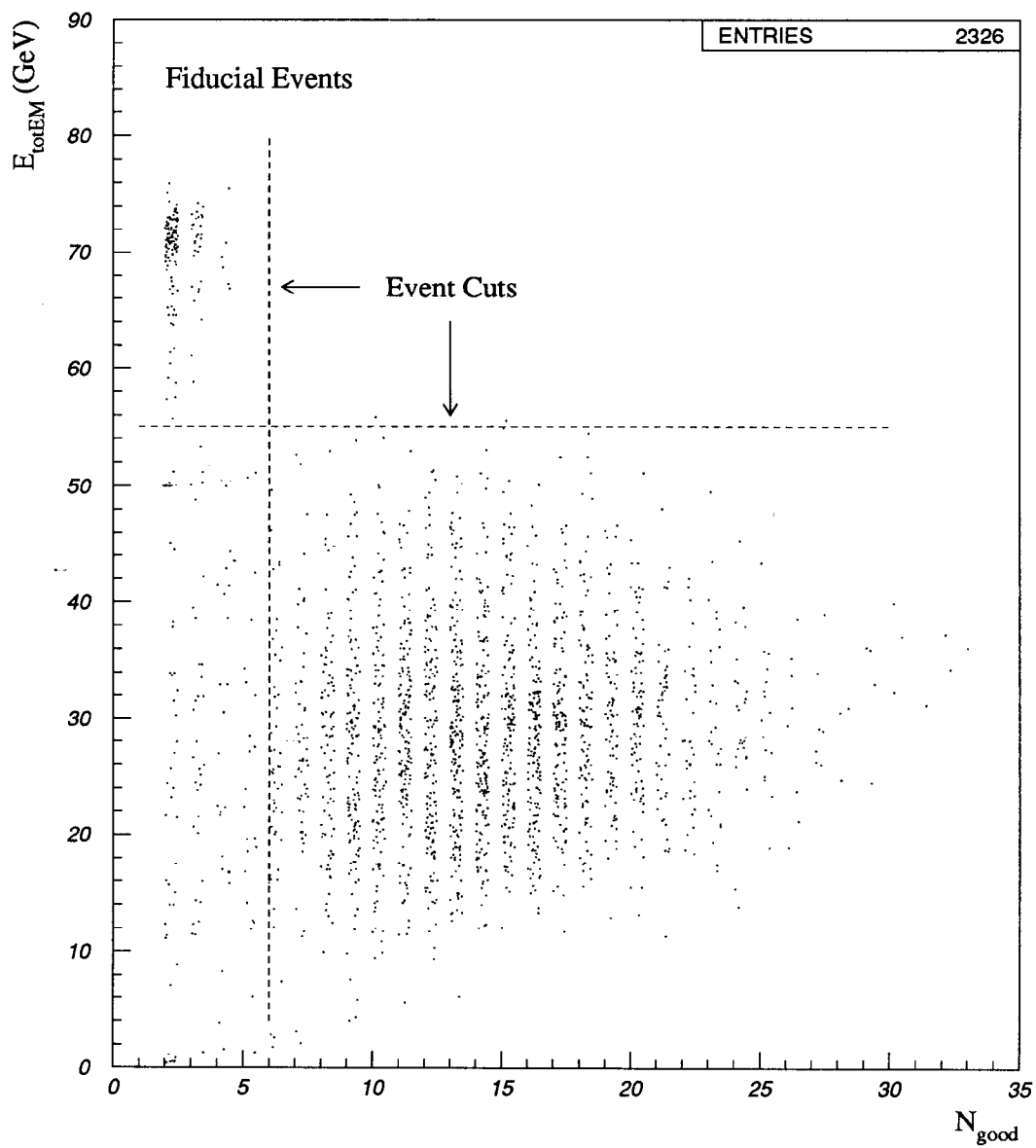
Figure 4-8 shows a plot of  $E_{totEM}$  vs.  $N_{good}$  for all events which pass the fiducial cuts. The event cuts are shown as dashed lines in the figure. The integer value of  $N_{good}$  is randomly scattered to as much as  $\frac{1}{2}$  more so the density of points is more clearly seen.

### 4.5.4 Comparison with Monte Carlo

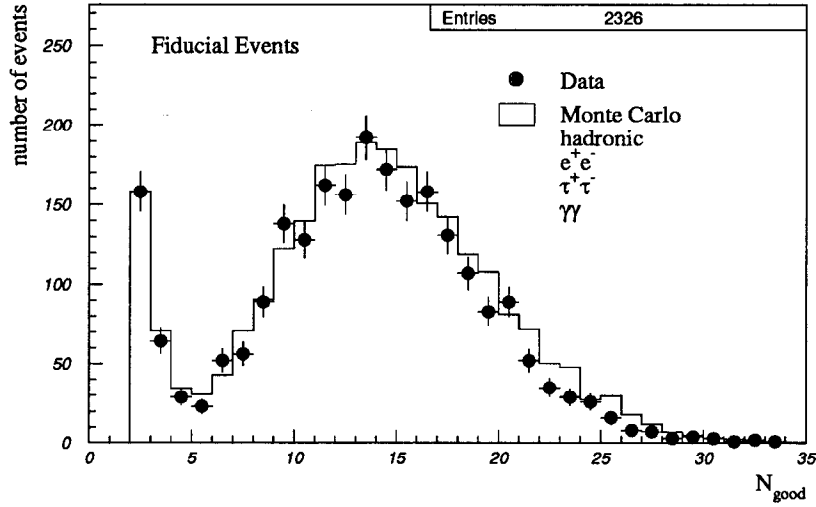
The following plots compare the data and Monte Carlo for the final cut variables.

Figure 4-9 shows the good cluster multiplicity  $N_{good}$  for fiducial events. This distribution demonstrates that the low multiplicity region is properly simulated. This is important for background determination.

Figure 4-10 is the distribution of  $E_{totEM}$  for all fiducial events which pass the cut  $N_{good} \leq 5$ . The final sample of events is all events above the 55 GeV cut. The peak from the wide angle Bhabha signal is clearly seen. The solid line histogram is the



**Figure 4-8:**  $E_{totEM}$  vs.  $N_{good}$   
 A scatter plot of  $E_{totEM}$  vs.  $N_{good}$  for events which satisfy the fiducial cuts.



**Figure 4-9:**  $N_{good}$  for fiducial events.  
The good cluster multiplicity for fiducial events for Monte Carlo and data.

absolute yield prediction from the signal and background processes as determined from the Monte Carlo. The  $\tau$  pair and hadronic event background components are shown as the hatched histogram and are primarily below the 55 GeV cut. The background from  $\tau$  pair events and hadronic events is determined to be  $0.87 \pm 0.22$  events and  $< 0.6$  events @ 95% confidence respectively. The largest background comes from the QED process  $e^+e^- \rightarrow \gamma\gamma$ . The prediction for the yield from this process is shown as the cross-hatched distribution under the main Bhabha peak. This process is essentially indistinguishable from a wide angle Bhabha event because no tracking information is used in this analysis. The prediction for the  $\gamma\gamma$  background is  $2.18 \pm 0.06$  events for a total of  $3.05 \pm 0.23$  events for all processes.

Figure 4-11 is the distribution of  $E_{totEM}$  for all events which pass all of the selection criteria. The uncorrected yield is 153 events. The overall efficiency for selecting wide angle Bhabha events in the fiducial region is determined from the Monte Carlo to be  $93.31 \pm 0.93\%$  and will be discussed in detail in the next chapter.

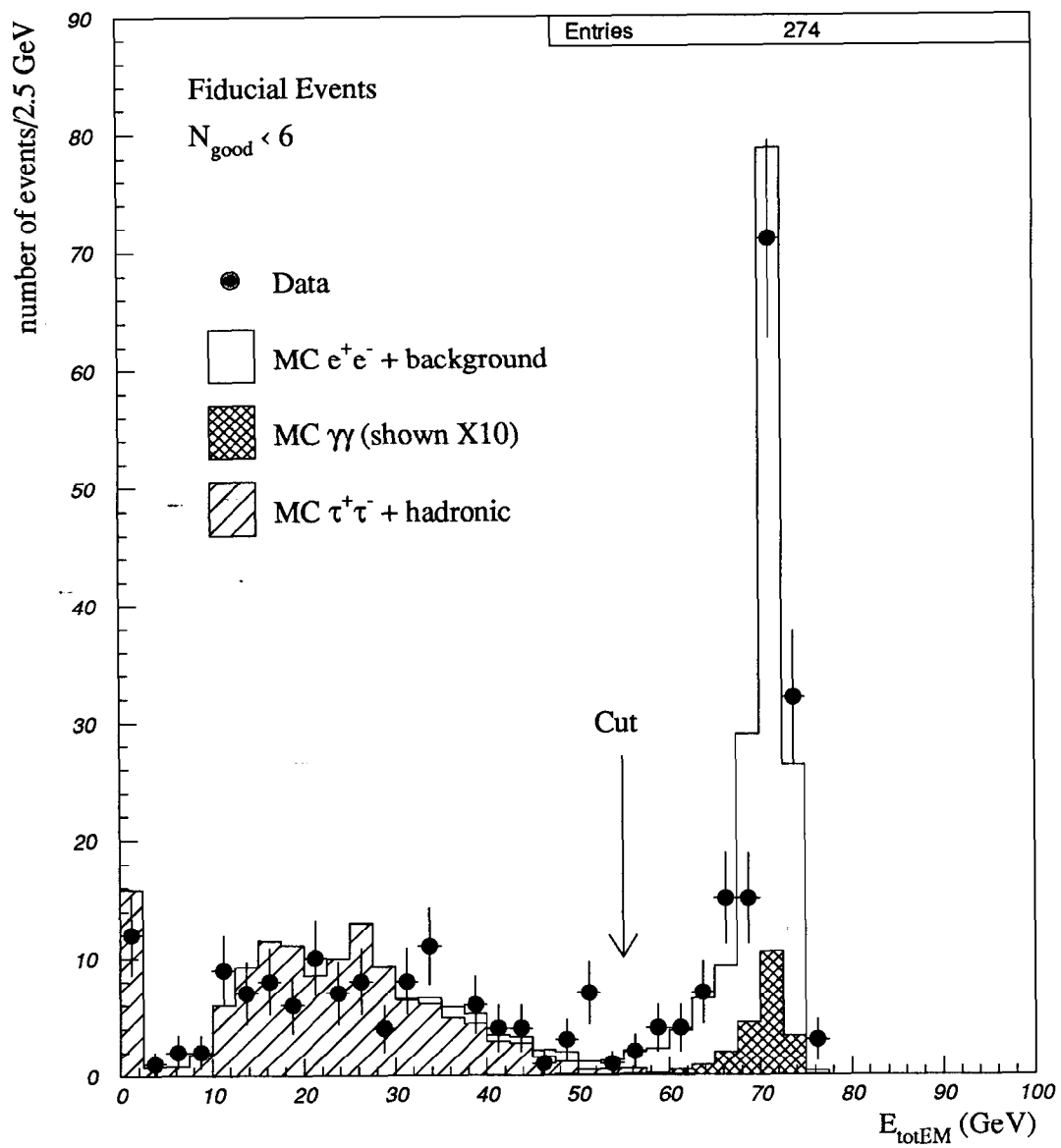


**Figure 4-10:**  $E_{\text{totEM}}$  for low multiplicity fiducial events  
 $E_{\text{totEM}}$  for low multiplicity fiducial events compared with the Monte Carlo prediction for  $e^+e^-$  and background processes.

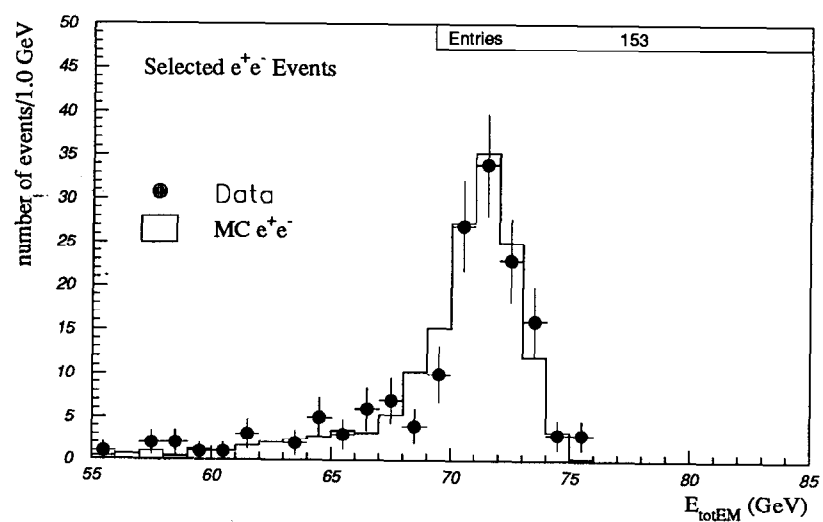


**Figure 4-11:**  $E_{totEM}$  for selected wide angle Bhabha events  
 $E_{totEM}$  for the final set of selected wide angle Bhabha events. It is compared with the Monte Carlo prediction.

# Chapter 5

## The Wide Angle Bhabha Cross Section

The cross section for wide angle Bhabhas into the fiducial region described in the previous chapter will be calculated from the yield and the integrated luminosity of the run. We will outline the corrections to the yield and the describe the integrated luminosity analysis.

### 5.1 The Cross Section

The cross section is determined from the following expression:

$$\sigma_{ee} = \frac{N_c}{\mathcal{L}} \quad (5.1)$$

where  $N_c$  is the corrected yield and  $\mathcal{L}$  is the integrated luminosity. The corrected yield is determined from the event yield,  $N_{tot}$  and the corrections  $N_b$ ,  $\epsilon$  and  $r$  by the

following expression

$$N_c = \frac{N_{tot} - N_b}{r \epsilon} \quad (5.2)$$

where  $N_b$  is the number of expected background events,  $r$  is the yield reduction due to the beam energy spread and  $\epsilon$  is the efficiency for detecting a fiducial wide angle Bhabha event during the time that the luminosity monitor is active and triggering.

## 5.2 Corrections to the Wide Angle Bhabha Yield

### 5.2.1 Efficiency

The overall efficiency is composed of the efficiency for triggering, the PASS 1 selection efficiency and the event cuts efficiency. The error on the efficiency due to the Monte Carlo simulation will be given at the end of this subsection.

#### Triggering

The efficiency for the SLD to record *as ENERGY triggers* events which satisfy the ENERGY trigger requirements can be studied by looking at hadronic events which have satisfied the tracking trigger [33]. The tracking trigger is based on information from the Central Drift Chamber. This is independent of the LAC ENERGY trigger and therefore can be used to check the efficiency of the ENERGY trigger. Of the 3527 hadronic events which satisfied the track trigger none failed to satisfy the ENERGY trigger [34]. This means that the ENERGY trigger was active and performing  $> 99.9\%$  of the time at 95% confidence. Therefore, no correction is made for the trigger active time. If there had been some events which had enough energy to satisfy the



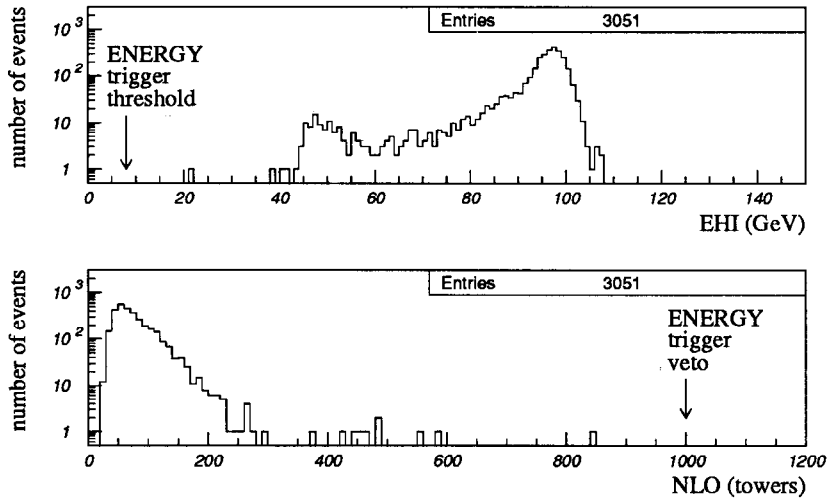


**Figure 5-1:** The ENERGY trigger quantities EHI and NLO for Monte Carlo  $e^+e^-$  events which satisfy the fiducial cuts at the generator level.

ENERGY trigger but hadn't *actually* satisfied the ENERGY trigger (because the trigger processor was busy or even off) then a correction would have to have been made.

The efficiency for the ENERGY trigger to be satisfied for a fiducial event is  $> 99.9\%$  at 95% confidence. This can be seen in Figure 5-1. The top plot is the Monte Carlo distribution for the trigger quantity EHI for events which have been identified at the generator level to satisfy the fiducial cuts. No events fail the 8 GeV trigger threshold. Note the lower peak at  $\sim 50$  GeV. This peak is due to one of the  $e^+$  or  $e^-$  entering the gap between the modules. This gap represents the biggest effect on the efficiency when the selection cuts are applied. Note also that the case of both  $e^+$  and  $e^-$  hitting the gap does not exist because the magnetic field bends the  $e^+$  and  $e^-$  in the opposite sense and thus creates an artificial acolinearity which prevents both from hitting the gap. The bottom plot is the trigger quantity NLO for the same events. There are no events above the 1000 tower veto.

## PASS 1 Selection

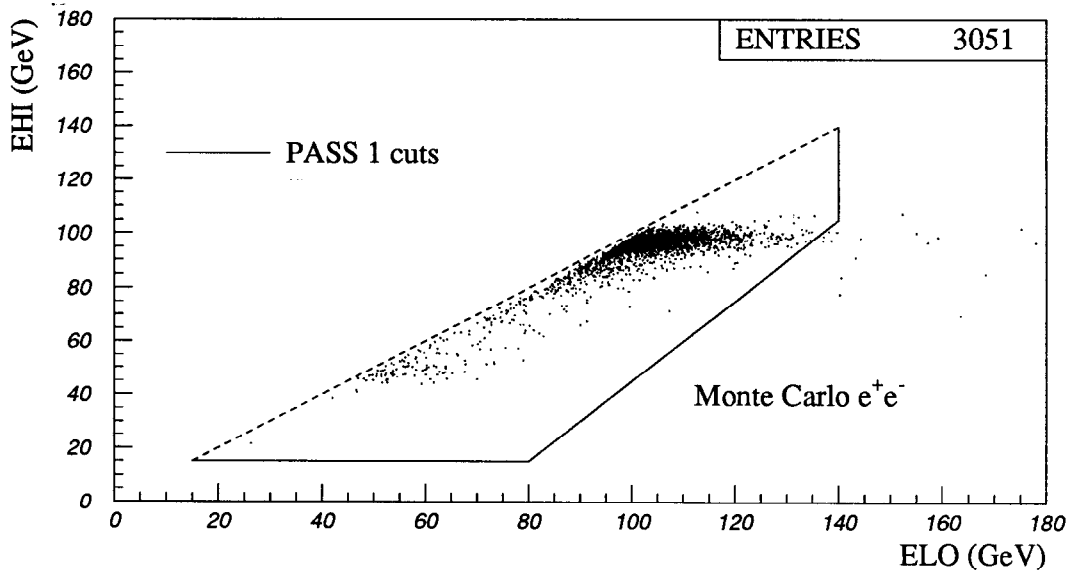
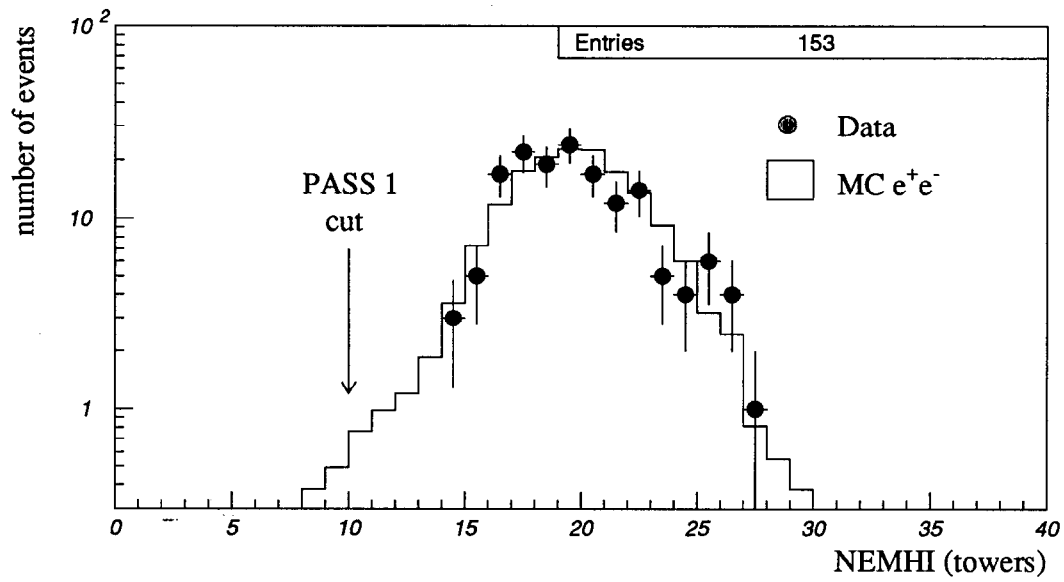
Figure 5-2 shows the PASS 1 selection variables for  $e^+e^-$  Monte Carlo events which have passed the fiducial cuts at the generator level. The top plot is a plot of NEMHI for data and  $e^+e^-$  Monte Carlo (the data have passed all cuts). The bottom plot (compare with Figure 4-4) is a plot of EHI vs. ELO for *fiducial* Monte Carlo events. The events to the right of the cuts (solid lines) are events which are rejected because there is too much beam background noise in the LAC. The efficiency of the PASS 1 selection for selecting fiducial events is  $98.53 \pm 0.22\%$  where the error is due to Monte Carlo statistics.

Figure 5-3 shows the trigger quantities EHI and ELO for *fiducial* monte carlo  $e^+e^-$  event. They are compared with the final set of data events. The dashed histogram in the bottom plot is for Monte Carlo events which do not have the backgrounds overlaid. It is clear that the backgrounds are necessary to properly model this distribution.

## Event Cuts

The fiducial cuts that are applied to the data should have little effect on the efficiency of the event cuts. This is because the  $\cos\theta$  distribution is essentially flat on the scale of the angular resolution and the  $\Theta_{acol}$  cut is on the tail of that distribution (see Figure 5-6). This hypothesis was tested with Monte Carlo data and found to be true. The effect of these cuts is  $< 0.1\%$ .

The main source of inefficiency from the event cuts is the cut on  $E_{totEM}$ . Figure 5-4 is similar to Figure 4-10 but in this case only the  $e^+e^-$  Monte Carlo events are compared to the data to more clearly show the energy distribution from the Monte Carlo. The cut at 55 GeV is  $94.94 \pm 0.41\%$  efficient for selecting fiducial  $e^+e^-$  events which have passed the PASS 1 cuts. The other event cut is the multiplicity cut of  $N_{good} \leq 5$ . That distribution is shown in Figure 5-5 for events which have passed the PASS 1 selection and the  $E_{totEM}$  cut. The efficiency for that cut is  $99.75 \pm 0.09\%$ .



**Figure 5-2:** The PASS 1 selection cuts NEMHI for Monte Carlo  $e^+e^-$  events (solid), and the EHI vs. ELO cuts on Monte Carlo  $e^+e^-$  events. The points in the top plot are for the final set of data events.

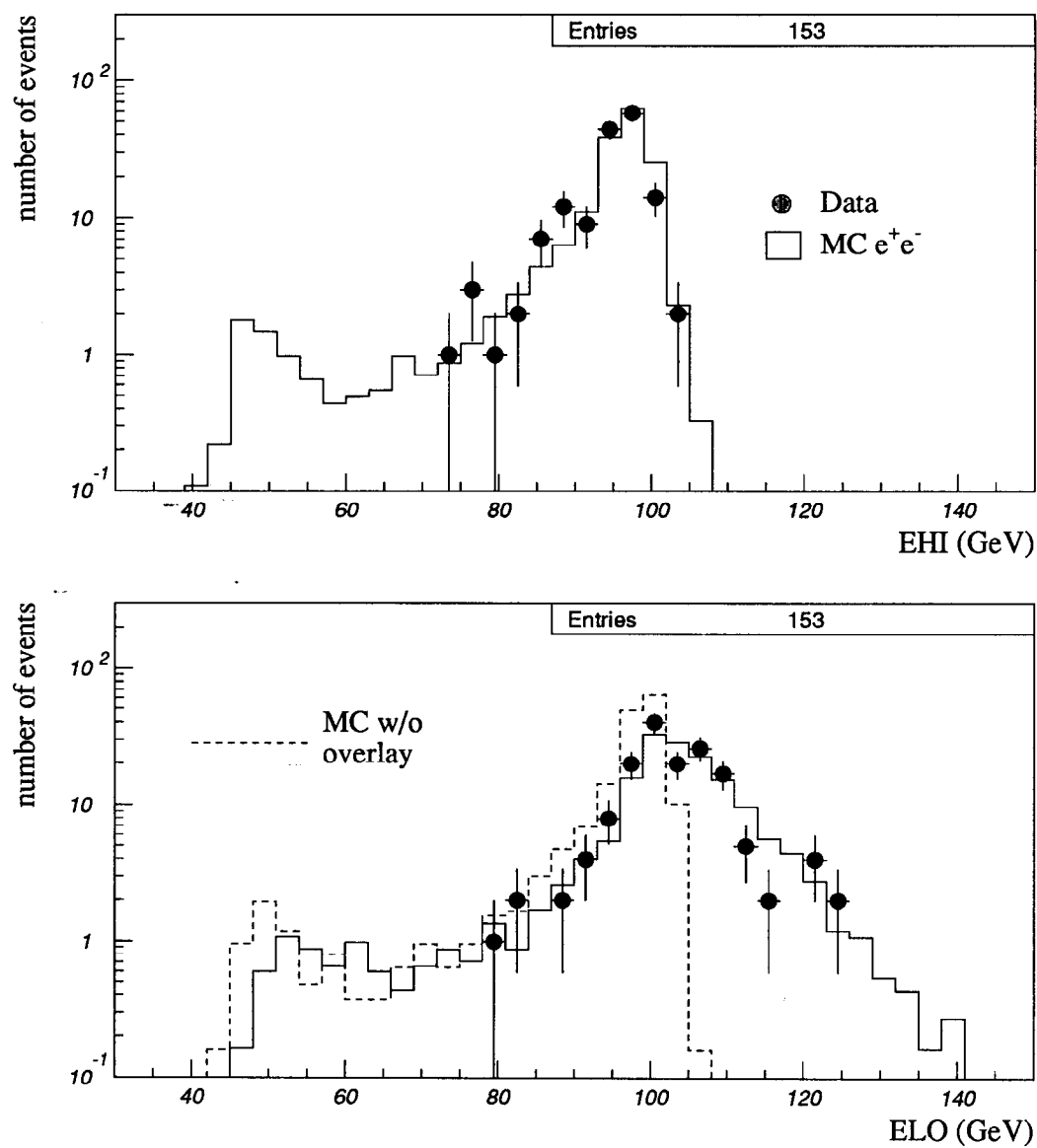


**Figure 5-3:** The trigger quantities EHI and ELO for Monte Carlo  $e^+e^-$  events compared with data which have passed all cuts. Dashed histogram in bottom plot is for Monte Carlo events without backgrounds overlaid.

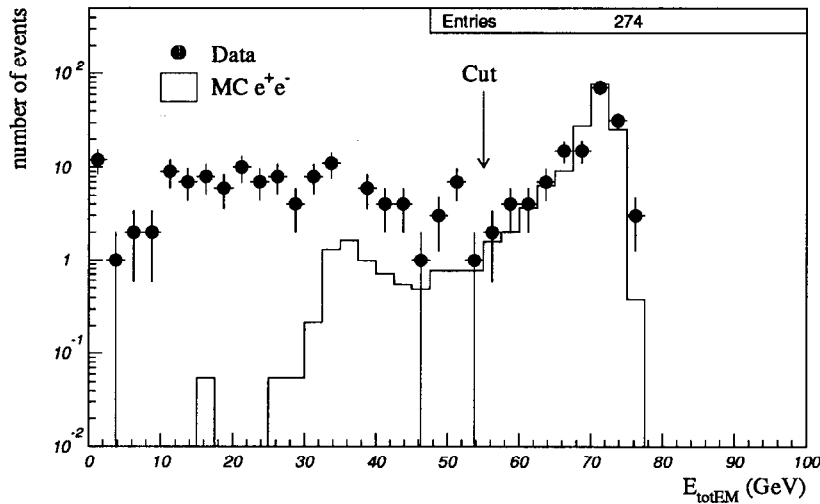


**Figure 5-4:**  $E_{totEM}$  for all events which pass the PASS 1 cuts.

The total efficiency for the event cuts is then  $94.71 \pm 0.42\%$ .

By combining the PASS 1 efficiency with the event cut efficiency, an overall efficiency for selecting fiducial wide angle Bhabha events is  $93.31 \pm 0.47\%$ .

### Summary

The errors on the efficiency are due to Monte Carlo statistics. In addition to that error there is an error due to the Monte Carlo itself. The error due to the tuning of the Monte Carlo is 0.26%. The tuning was done on the main Bhabha energy peak to match the data with the Monte Carlo. An error of 0.25% is included to account for any discrepancy between the data and Monte Carlo in the multiplicity distribution (this is 1 minus the multiplicity cut efficiency). Finally, there is an error of 0.59% due to the description of the LAC modules whose inter-module gap have the largest impact on the  $E_{totEM}$  cut efficiency. The total error is then 0.69%.

The efficiency of each stage for detecting and identifying a wide angle Bhabha is given in Table 5.1

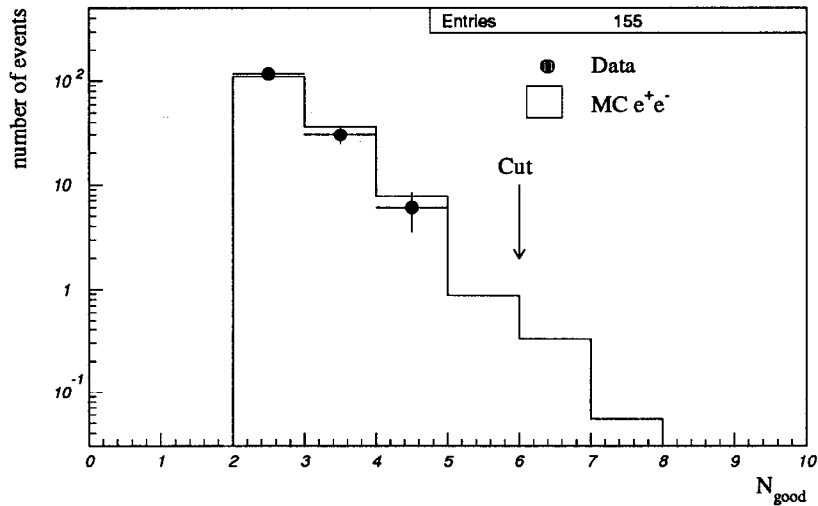


**Figure 5-5:**  $N_{good}$  for all events which pass the PASS 1 cuts.

	Efficiency (%)	Error
Triggering	100.00	< 0.1
PASS 1 Selection	98.53	0.22
Event Cuts	94.71	0.42
Monte Carlo	—	0.69
<i>TOTAL</i>	93.31	0.93

**Table 5.1:** Efficiencies for detecting and identifying wide angle Bhabhas.

### 5.2.2 Backgrounds

The backgrounds from physics processes have been discussed in section 4.5 and are listed in Table 5.2 as well as an *estimate* for unmodeled backgrounds such as beam related noise or electronics problems. The estimate comes from the observing the distribution of  $\Theta_{acol}$  in Figure 5-6. All cuts have been applied except the cut on  $\Theta_{acol}$ . One can see that there are two separate populations, one from the wide angle Bhabhas and one from unmodeled background events. From the distribution it can be seen that the unmodeled background is entirely separated from the wide angle Bhabha events.

The error for the background from hadronic events is reduced from the upper limit

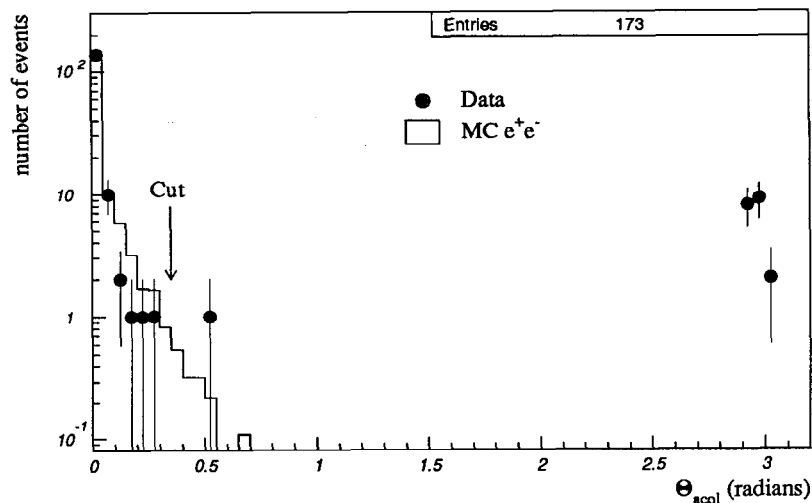


**Figure 5-6:**  $\Theta_{acol}$  for events which pass all other cuts.

quoted in section 4.5. This is achieved by extrapolating the spectrum of energy for the Monte Carlo hadronic events above the 55 GeV cut. The confidence limit has been adjusted to correspond to a 1 sigma upper limit.

	Expected number	Error
$e^+e^- \rightarrow \gamma\gamma$	2.18	0.06
$e^+e^- \rightarrow \tau^+\tau^-$	0.87	0.22
$e^+e^- \rightarrow q\bar{q}$	0.0	< 0.1
Unmodeled	0.0	—
<i>TOTAL</i>	3.05	0.23

**Table 5.2:** The expected number of background events from different processes.

### 5.2.3 Beam Energy Spread

In order to extract the partial width,  $\Gamma_{ee}$ , it is necessary to measure the cross section at a *known*  $E_{cm}$ . A spread in the  $E_{cm}$  distribution will mean that the events are sampling different parts of the cross section. In addition, if the second derivative of the cross section with respect to  $E_{cm}$  is non-zero, then a spread in  $E_{cm}$  will lead to an average cross section (averaged over the  $E_{cm}$  distribution) that will be different from

the cross section at the average energy.

Given that the average  $E_{cm}$  for the SLC was 91.55 GeV and the chosen fiducial cuts for this analysis, the  $E_{cm}$  spread will produce a reduction in the yield (relative to the expectation for a monochromatic  $E_{cm}$ ) because the second derivative of the cross section for wide angle Bhabhas into the fiducial region is negative at that energy. The cross section from MIBA is plotted as a function of  $E_{cm}$  in Figure 5-7.

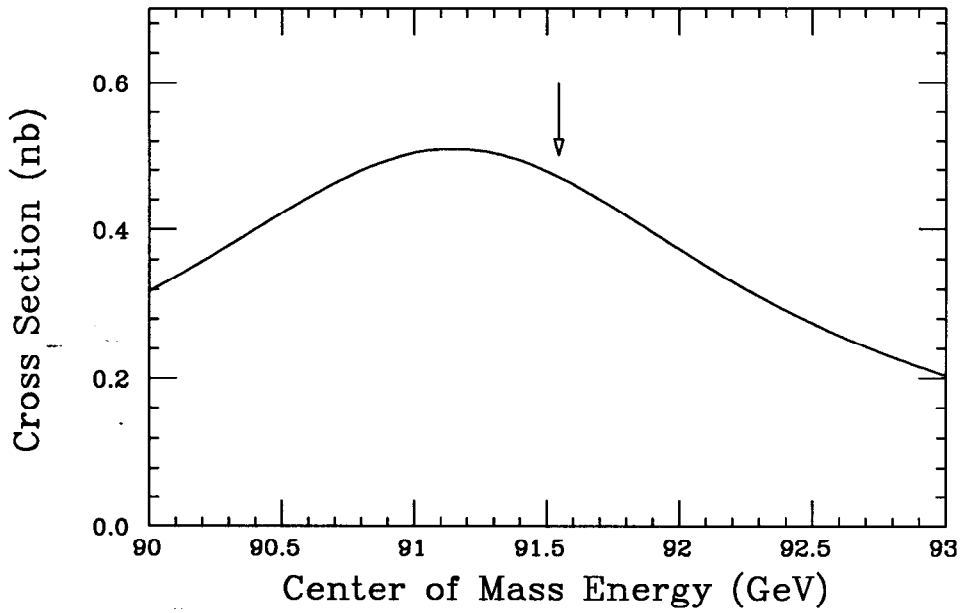


**Figure 5-7:** The Cross Section for  $e^+e^-$  events into the fiducial region as a function of the center of mass energy,  $E_{cm}$ . The arrow indicates the  $E_{cm}$  of the collisions that the SLC was producing.

The beam energy rms for 1992 was 0.25% for the  $e^-$  beam and 0.2% for the  $e^+$  beam and the pulse to pulse jitter of the beams is 0.1% [35]. There is not a large amount of data on the shape and spread of the beam so we will make loose assumptions about them.

Figure 5-8 shows  $E_{cm}$  for the case of gaussian beam energy profiles and rms spreads of the beams of 0.2% or 0.3%.

The reduced cross section  $\sigma_r$ , is calculated according to eq. (5.3)



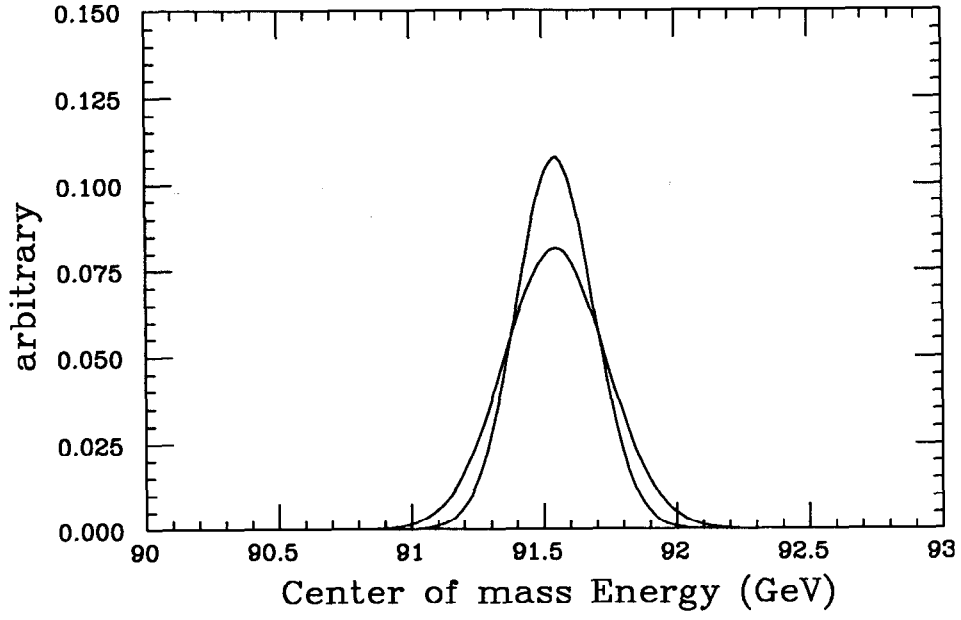


**Figure 5-8:** The center of mass energy distribution,  $E_{cm}$  for the SLC for the case of a 0.2% or 0.3% beam energy rms.

$$\sigma_r = \int \sigma_{ee}(E_{cm})P(E_{cm})dE_{cm} \quad (5.3)$$

where  $P(E_{cm})$  is the normalized center of mass energy spectrum.

The reduction factor  $r$ , is then given by eq. (5.4)

$$r = \frac{\sigma_r}{\sigma_0} \quad (5.4)$$

where  $\sigma_0$  is the  $e^+e^-$  cross section at the mean energy of the  $P(E_{cm})$  distribution.

By varying the hypothesis which is made of  $P(E_{cm})$ , (position, shape and rms) the following reduction factor is obtained:

$$r = 0.9907 \pm 0.0027, \quad (5.5)$$

where the error is half of the full variation of the  $P(E_{cm})$  hypotheses, namely that the beam energy distribution was either flat or gaussian, that the rms of the distribution was 0.2 or 0.3% and that mean  $E_{cm}$  is  $91.55 \pm 0.02$  GeV.

### 5.3 Integrated Luminosity

The integrated luminosity is determined from small angle Bhabha scattering events which are recorded in the luminosity monitor [36]. The selected events are classified by the location of the two showers in the luminosity monitor. The two fiducial regions, precise and gross, are defined by limits on the polar angle of the shower. The precise region has a polar angular range of 36.0 to 62.7 mrad. The gross region includes the whole luminosity monitor (28.9 to 65 mrad) excluding the precise region. If both showers in the event lie inside of the precise fiducial then the event is classified as a *precise* event. If one shower is in the precise region and one is in the gross region then the event is classified as a *gross* event. Events where both showers are detected in the gross region are not considered.

This sort of classification is necessary owing to the strong dependence of the cross section on the polar angle. If there is a small displacement in the detectors either with respect to each other or to the interaction point, then some *precise* events (mostly events with both showers near the inner edge of the precise fiducial region) will be recorded as *gross* events. In addition, some events which would otherwise not have been considered (mostly events with both showers just outside of the precise region) will be recorded also as *gross* events. In fact, the number of *precise* events lost is equal to half of the number of *gross* events gained in the limit of small displacement.

An *effective* number of events can be determined by adding half of the *gross* events to the *precise* events.

$$n_{eff} = n_{precise} + \frac{n_{gross}}{2} \quad (5.6)$$

In this way, the effect of small displacements cancel to first order and only effect the result to second order.

This procedure is simulated using a Monte Carlo which takes into account all of the detector conditions and which uses event generators to simulate initial and final state radiation effects. The events are generated with a final state polar angle range which is larger than the luminosity detector and whose cross section ( $\sigma_{theory}$ ) is well known theoretically. The effective cross section is given by:

$$\sigma_{eff} = \sigma_{theory} \frac{n_{effmc}}{n_{generated}} \quad (5.7)$$

where  $n_{effmc}$  is the effective number of events from the Monte Carlo given by eq. (5.6) and  $n_{generated}$  is the total number of events generated for the simulation.

The integrated luminosity,  $\mathcal{L}$ , is then given by:

$$\mathcal{L} = \frac{n_{eff}}{\sigma_{eff}} \quad (5.8)$$

The analysis is detailed in reference [36].

A fiducial set of runs were used for both the wide angle Bhabha analysis and the luminosity analysis (representing 92% of the run). The result for the integrated

luminosity is:

$$\mathcal{L} = 354.4 \pm 2.4 \pm 3.6 \text{ nb}^{-1} \quad (5.9)$$

where the first error is statistical and the second is systematic. The systematic error is comprised of a total experimental error of  $3.1 \text{ nb}^{-1}$  and theoretical error of  $1.8 \text{ nb}^{-1}$

It is noted that this  $\mathcal{L}$  is integrated over the "on time" of the ENERGY trigger. This is done automatically since the ENERGY trigger and the trigger which records the luminosity Bhabha events have identical detector requirements and therefore have the same detector dead time.

## 5.4 The Measured Cross Section

Using equation eq. (5.1) the total cross section  $\sigma_{ee}$ , at  $E_{cm}$  of 91.55 GeV into the fiducial region is:

$$\sigma_{ee} = 457.7 \pm 37.8 \pm 7.2 \text{ pb} \quad (5.10)$$

where the first error is statistical and the second is the combined systematic error.

The systematic errors of the cross section measurement are shown in Table 5.3

	Error (pb)
$\mathcal{L}$	5.6
Efficiency	4.3
Beam Spread	1.0
Backgrounds	0.7
<i>TOTAL</i>	7.2

**Table 5.3:** The systematic errors in the measurement of the cross section.

# Chapter 6

## Results

The partial decay width of the  $Z^0 \rightarrow e^+e^-$ ,  $\Gamma_{ee}$ , will be determined from the cross section measurement of the previous chapter. MIBA will be used to calculate the cross section into the fiducial region at  $E_{cm} = 91.55$  GeV as a function of  $\Gamma_{ee}$ . The result for  $\Gamma_{ee}$  is obtained by comparing the measured cross section with the curve generated by MIBA. This result will be combined with the SLD result for  $A_{LR}$  to extract the effective vector and axial-vector couplings of the electron,  $\bar{g}_v^e$  and  $\bar{g}_a^e$ .

### 6.1 $\Gamma_{ee}$

The fixed inputs for MIBA are the recent precision results for the mass and width of the  $Z^0$  from LEP [6] as well as the experimental settings of this analysis which are the fiducial cuts and  $E_{cm}$ .  $\Gamma_{ee}$  is varied to produce a theoretical curve of the cross section,  $\sigma_{ee}$ , vs.  $\Gamma_{ee}$ . This is shown in Figure 6-1. The curve is essentially quadratic because most of the cross section (for the fiducial cuts) is due to the resonance of the  $Z^0$  and little is due to the  $t$  - *channel* or interference contribution.

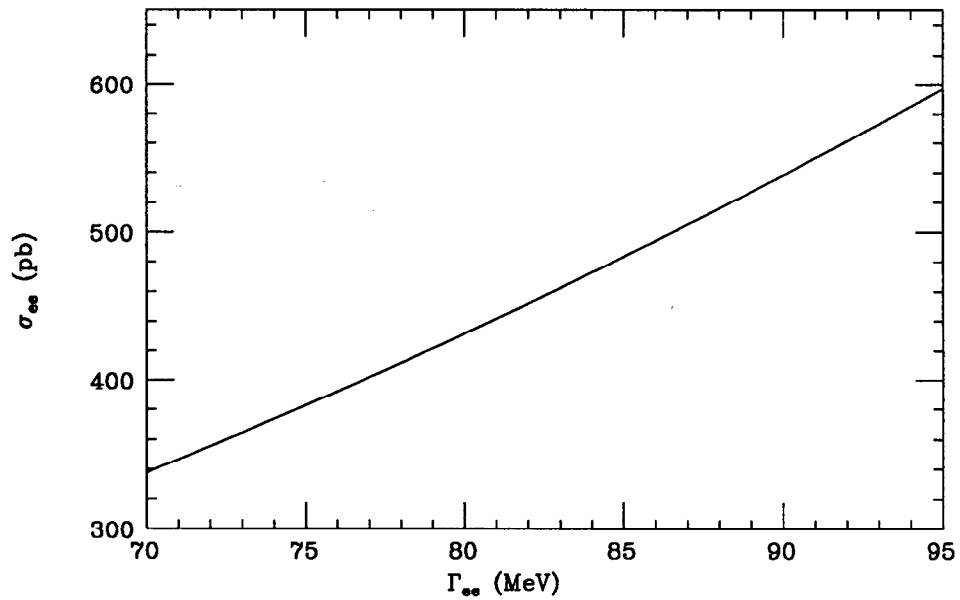


**Figure 6-1:** The theoretical dependance of the cross section on  $\Gamma_{ee}$ .

### 6.1.1 Cross Section Fit to $\Gamma_{ee}$

With the cross section measurement of the previous chapter it is now possible to extract the partial width  $\Gamma_{ee}$ . Figure 6-2 is a plot of the theoretical curve with the cross section measurement drawn onto it showing where the measurement intersects the curve. The statistical and systematic errors of the cross section measurement are also shown. The vertical lines indicate what the central value is, and what the errors are for  $\Gamma_{ee}$ .

The result for the  $e^+e^-$  decay width of the  $Z^0$ ,  $\Gamma_{ee}$ , is

$$\Gamma_{ee} = 82.4 \pm_{3.7}^{3.6} \text{ MeV} \quad (6.1)$$

where only the statistical error is quoted. This result is in agreement with more precise measurements from LEP experiments(ref). The systematic error due to the cross

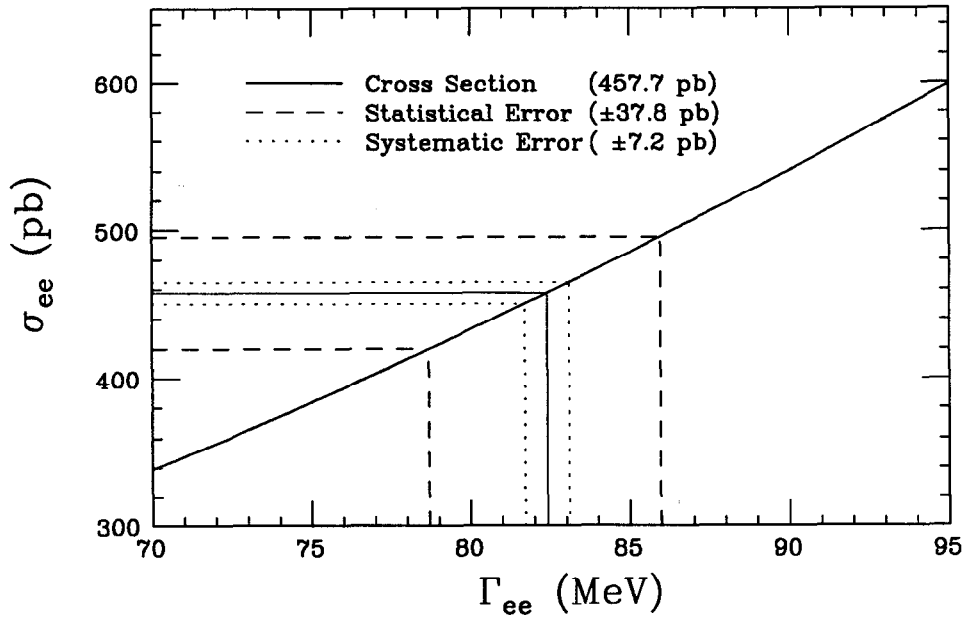


**Figure 6-2:** The measured cross section projected onto the theoretical curve.

section systematic error is 0.7 MeV. Additional systematic errors will be discussed in the next subsection.

### 6.1.2 Systematic Errors

In addition to the systematic error of the cross section measurement one must take into account the errors of the theoretical curve in Figure 6-1. The most important error associated with the curve is the experimental uncertainty in  $E_{cm}$ . Since the calculation depends on  $E_{cm}$  the curve is generated for the central value of  $E_{cm}$  (as in Figure 6-1) and for the value of  $E_{cm} \pm 20$  MeV. This variation of  $E_{cm}$  leads to roughly 0.7% variation of the cross section for a given  $\Gamma_{ee}$ . This is as large as it is because  $E_{cm}$  is above the peak and consequently in a region where the cross section is changing. The error is much reduced when the  $E_{cm}$  is set to the  $Z^0$  peak energy (91.28 GeV).

It is also necessary to to account for the error due to the accuracy of the calcula-



tion. This is quoted as 0.5% [10]. There is also a 0.5% error due to the uncertainty in  $\Gamma_Z$  and  $M_Z$ . These errors result in a family of curves with which to compare the result of the cross section measurement. These curves are shown in Figure 6-3. The cross section measurement central value is drawn to intersect the curves, determining the systematic errors.

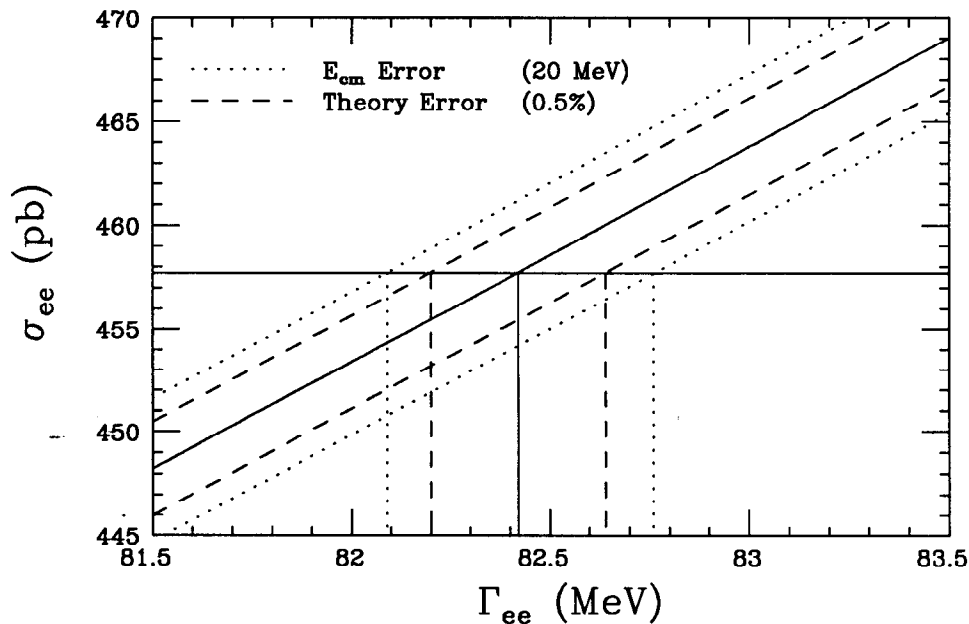


**Figure 6-3:** The errors to the theoretical curve with the cross section measurement projected to indicate the systematic errors on  $\Gamma_{ee}$ .

The systematic errors for  $\Gamma_{ee}$  are summarized in Table 6.1

	Error (MeV)
$\sigma_{ee}$ systematic	0.69
$E_{cm}$	0.34
QED	0.22
$\Gamma_Z, M_Z$	0.22
<i>TOTAL</i>	0.83

**Table 6.1:** The systematic errors in the measurement of the  $\Gamma_{ee}$ .

## 6.2 Comparison with LEP

The 4 LEP experiments, with their larger statistical samples and competitive detectors can measure  $\Gamma_{ee}$  more precisely. They are beginning to test the Theory at the loop level. The results of their measurements are now being used to constrain the value of the top quark mass [6]. Some recent results for  $\Gamma_{ee}$  from the four LEP experiments ALEPH, DELPHI<sup>1</sup>, L3, and OPAL are presented in Table 6.2.

Experiment	$\Gamma_{ee}$ (MeV)	error (MeV)
ALEPH [37]	84.43	0.60
DELPHI [38]	82.4	1.2
L3 [39]	83.0	0.6
OPAL [40]	83.63	0.53

**Table 6.2:** Recent results from LEP for  $\Gamma_{ee}$

One can see that even these more precise results are in agreement with the tree level prediction of  $\Gamma_{ee}$ .

## 6.3 $\bar{g}_v^e$ and $\bar{g}_a^e$

Given the measurement of  $\Gamma_{ee}$  and the result for  $A_{LR}$  [1] it is now possible to extract  $\bar{g}_v^e$  and  $\bar{g}_a^e$ . Using eq.(1.7) the couplings are determined to be:

$$\bar{g}_v^e = -0.024 \pm 0.011 \quad (6.2)$$

$$\bar{g}_a^e = -0.498 \pm 0.011 \quad (6.3)$$

---

<sup>1</sup>The DELPHI result is older than the other three. A more recent result is being prepared for publication.

Figure 6-4 shows the 1-sigma contours of  $\bar{g}_v^e$  and  $\bar{g}_a^e$  in the  $\bar{g}_v^e - \bar{g}_a^e$  plane for the  $\Gamma_{ee}$  and  $A_{LR}$  measurements.

The overlap of the two regions determines  $\bar{g}_v^e$  and  $\bar{g}_a^e$ . A joint estimate of  $\bar{g}_v^e$  and  $\bar{g}_a^e$  leads to the 68.3% contour which is shown as the dotted circle (since the magnitude of the errors are equal, the contour appears to be a circle).

## 6.4 Summary of Results

We have measured the wide angle Bhabha cross section at  $E_{cm} = 91.55$  GeV into the fiducial region of  $|\cos \theta| < 0.407$  and  $\Theta_{acol} < 20^\circ$ . We find:

$$\sigma_{ee} = 457.7 \pm 37.8 \pm 7.2 \text{ pb} \quad (6.4)$$

where the first error is statistical and the second is the total systematic.

From this measurement and the precision  $Z$  mass and width measurements from LEP we determine  $\Gamma_{ee}$  to be:

$$\Gamma_{ee} = 82.4 \pm_{3.7}^{3.6} \pm 0.8 \text{ MeV} \quad (6.5)$$

By combining this result with the SLD result for  $A_{LR}$  we can extract  $\bar{g}_v^e$  and  $\bar{g}_a^e$  for the electron. We find:

$$\bar{g}_v^e = -0.024 \pm 0.011 \quad (6.6)$$

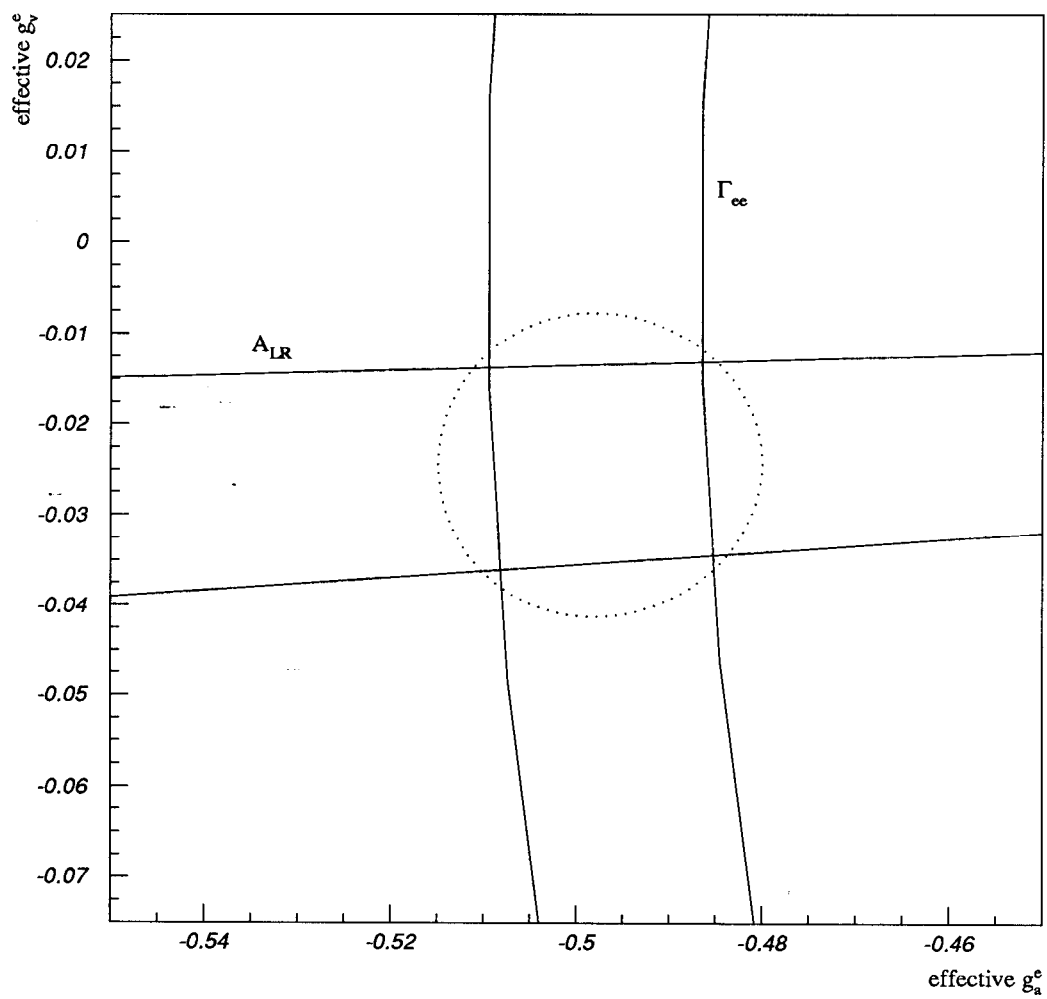


**Figure 6-4:** The 1-sigma contours of  $\bar{g}_v^e$  and  $\bar{g}_a^e$  from  $\Gamma_{ee}$  and  $A_{LR}$ . The dotted circle is the 68.3% confidence contour for the joint estimation of  $\bar{g}_v^e$  and  $\bar{g}_a^e$ .

$$\bar{g}_a^e = -0.498 \pm 0.011 \quad (6.7)$$

The measurements presented here represents a tree level test of the Standard Model of Electroweak Interactions. The value for  $\Gamma_{ee}$  predicted in section 1.5 (83.47 MeV) is within the errors of the measurement. The partial width,  $\Gamma_{ee}$  is most sensitive to the axial-vector coupling constant,  $\bar{g}_a^e$ . It is determined with a precision of 2.2% to be  $-\frac{1}{2}$  as predicted by the Theory (see Table 1.1).

## 6.5 Prospects

Clearly this result is statistics limited and therefore the simplest way to improve the result is to increase the data sample. The 1993 SLD physics run has just recorded roughly 5 times what was recorded in 1992. In addition, the Monte Carlo is improving which will allow a larger  $\cos \theta$  acceptance and therefore improved statistical precision (estimated error  $\simeq 1.0$  MeV).

The dominant systematic errors are the integrated luminosity, the efficiency, and the center of mass energy. The latter will improve because the 1993 run was taken at  $E_{cm} = 91.28$  GeV which is the peak of the cross section. This greatly reduces the uncertainty in the theoretical curve of the cross section vs.  $\Gamma_{ee}$ . The integrated luminosity error will improve somewhat because some of its error is statistical. Some improvement will come from a better understanding of the detector with more analysis and statistics. With more statistics, tighter constraints could be placed on the distributions used to determine the efficiency, which should lead to a reduction in the error on the efficiency.

Another approach to measuring  $\Gamma_{ee}$  is to measure the angular distribution of the wide angle Bhabha events [41]. DMIBA is a fitting routine written by one of the

authors of MIBA (and another author) which uses the increasing yield at smaller angles to effectively measure the integrated luminosity. This eliminates the need for the integrated luminosity (with a small increase in statistical error) and also reduces the sensitivity to the efficiency since most of it is polar angle independent.

The increased polarization of the 1993 run ( $\sim 62\%$ ) will also allow for a measure of  $A_{LR}$  using the wide angle Bhabha events. This can be achieved by measuring  $\Gamma_{ee}$  for the left and right handed beams separately [32]. In this way  $\bar{g}_v^e$  and  $\bar{g}_a^e$  can be measured using only the wide angle Bhabha events.

# Appendix A

## SLC Muon Pattern Recognition

Muons from the SLC can deposit large amounts of energy in the LAC which can make the triggering of the SLD difficult. In addition, the background clusters which these muons create can impair event analysis. We will describe the algorithm which identifies SLC muon induced clusters in the LAC barrel. This algorithm led to an improved ENERGY trigger for the SLD as well as an improved PASS 1 selection filter<sup>1</sup> for hadronic and wide angle Bhabha events (described in sections 4.1 and 4.2). It has also been incorporated into the SLD calorimeter reconstruction for the purpose of event analysis.

### A.1 The Algorithm

Each cluster is a grouping of tower hits. The arrangement of hits is examined to determine if the cluster has been induced by an SLC muon. Since SLC muons travel parallel to the beam line they will deposit energy in *strings* of hits parallel to the LAC barrel axis (see Figure 4-1). This distinguishing feature can be quantified by

---

<sup>1</sup>In 1993, the PASS 1 selection variable NEMHI was added to the ENERGY trigger.

the number of pairs of hits in the cluster that are in the *same* layer (EM1,EM2,HD1 or HD2) and have the *same* azimuthal position and occupy *adjacent* polar positions (in other words they touch in the direction of the LAC barrel axis). We will call this the number of longitudinal pairs,  $n_l$ , where longitudinal is in reference to the direction of the SLC muon.

The complimentary pair definition is those hits that have the same polar position but are adjacent in their layer and or azimuthal position. We will refer to this number of pairs as  $n_t$  for the number of transverse pairs.

For any given tower, the number of possible transverse pairs is 8 (ignoring the confusing EM/HAD segmentation change) while the number of possible longitudinal pairs is 2. Therefor, in normal clusters (for example one which was induce by a particle incident on the LAC from the interaction point) we expected that on average  $n_t = 4 \times n_l$ . We also expect that an (ideal) SLC muon induced cluster will have  $n_t = 0$  and  $n_l = n_h - 1$  where  $n_h$  is the number of hits in the cluster.

The requirement for a cluster to be flagged as an SLC muon is then the following:

- $n_l \geq 2$
- $n_l \geq n_t + 2$
- $n_t \leq 20$

Figure A-1 shows a scatter plot of  $n_t$  vs.  $n_l$  for clusters in a loosely selected set of hadronic events [42]. The upper plot shows a wide range of pairs and the bottom plot is a narrow range near zero. This plot shows the results for the coarse clusters from the first stage of clustering (see section 4.3). Note the large band of points which have a slope of roughly 4 as expected from normal clusters and jets. The points along the bottom axis of the top plot represent the muon clusters which have low  $n_t$  and large  $n_l$ . The solid lines represent the cuts. Any cluster which lies below the cuts is



flagged as a muon induced cluster from the SLC. It is emphasized that the pattern recognition does not make use of the ADC count of the tower.

The bottom plot shows a close-up of the top plot to demonstrate the clarity with which the muon induced clusters can be separated from normal clusters. The smallest cluster (in terms of number of hits) which can be identified has three hits. These hits must line up and have no transverse pairs. If there are three longitudinal pairs then the cluster is allowed one transverse pair etc. The cut appears as a zigzag because the variables are integer and are plotted in boxes to reveal the density of points.

The limit of  $n_t \leq 20$  is in place to avoid flagging real clusters which have a muon or muons attached. Any cluster which lies above the cuts is examined in the same way after the those clusters have been refined.

Figure A-2 shows a scatter plot of  $n_t$  vs.  $n_l$  for all clusters above the cuts in Figure A-1. One can see that this scatter plot has fewer points on the right side of the plot. This is because the large clusters have been broken up into smaller ones. Consequently some of the normal clusters which had muon induced hits attached have been separated. The bottom plot demonstrates this by revealing some small muon induced clusters below the cuts.

Figure A-3 is a plot of all coarse clusters in the small angle Bhabha events recorded by the LMSAT. These events will not have anything in the LAC except for the backgrounds that were experienced during the run. One can see that most of the clusters are from the SLC muons.

Finally, Figure A-4 shows an event display of a hadronic event after the removal of the SLC muon induced events. Figure A-5 shows a display of the removed clusters.

SLC muons which penetrate the endcap LAC will closely resemble a muon which came from the IP. These muons can be identified in the LAC by recognizing the characteristic pattern of minimum ionizing energy and hit multiplicity in the four LAC layers.

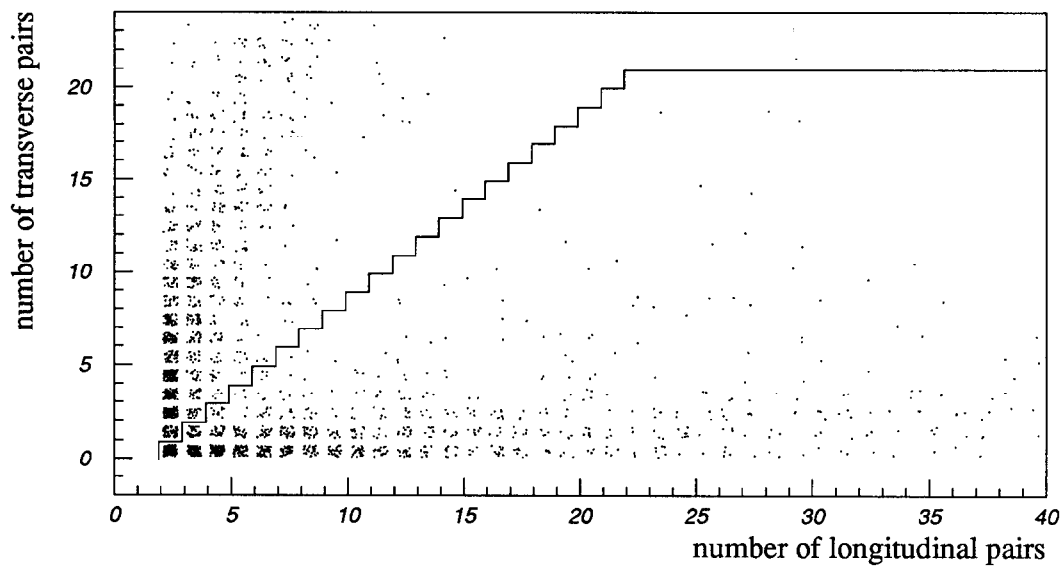
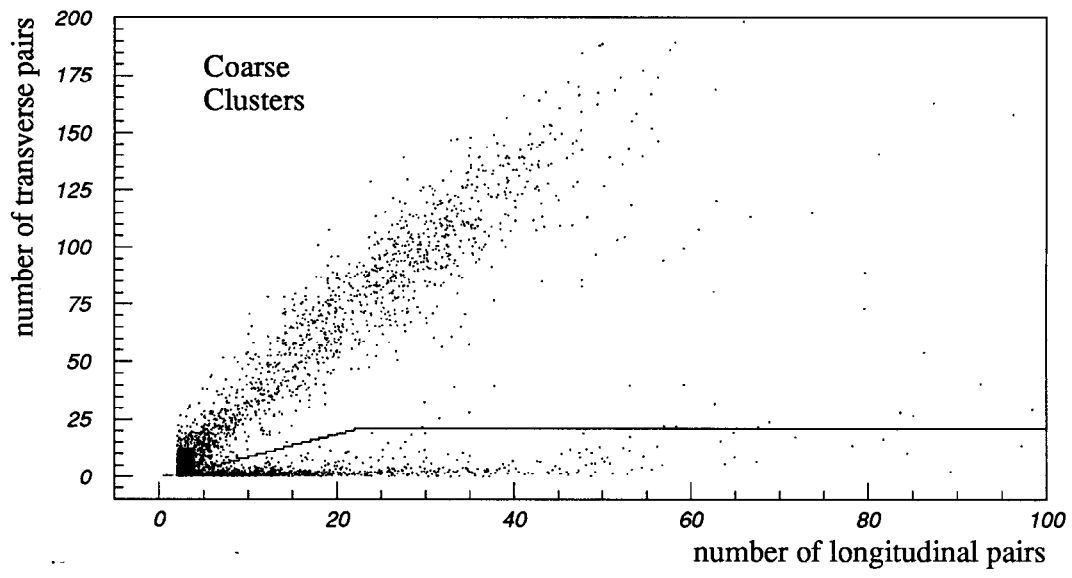
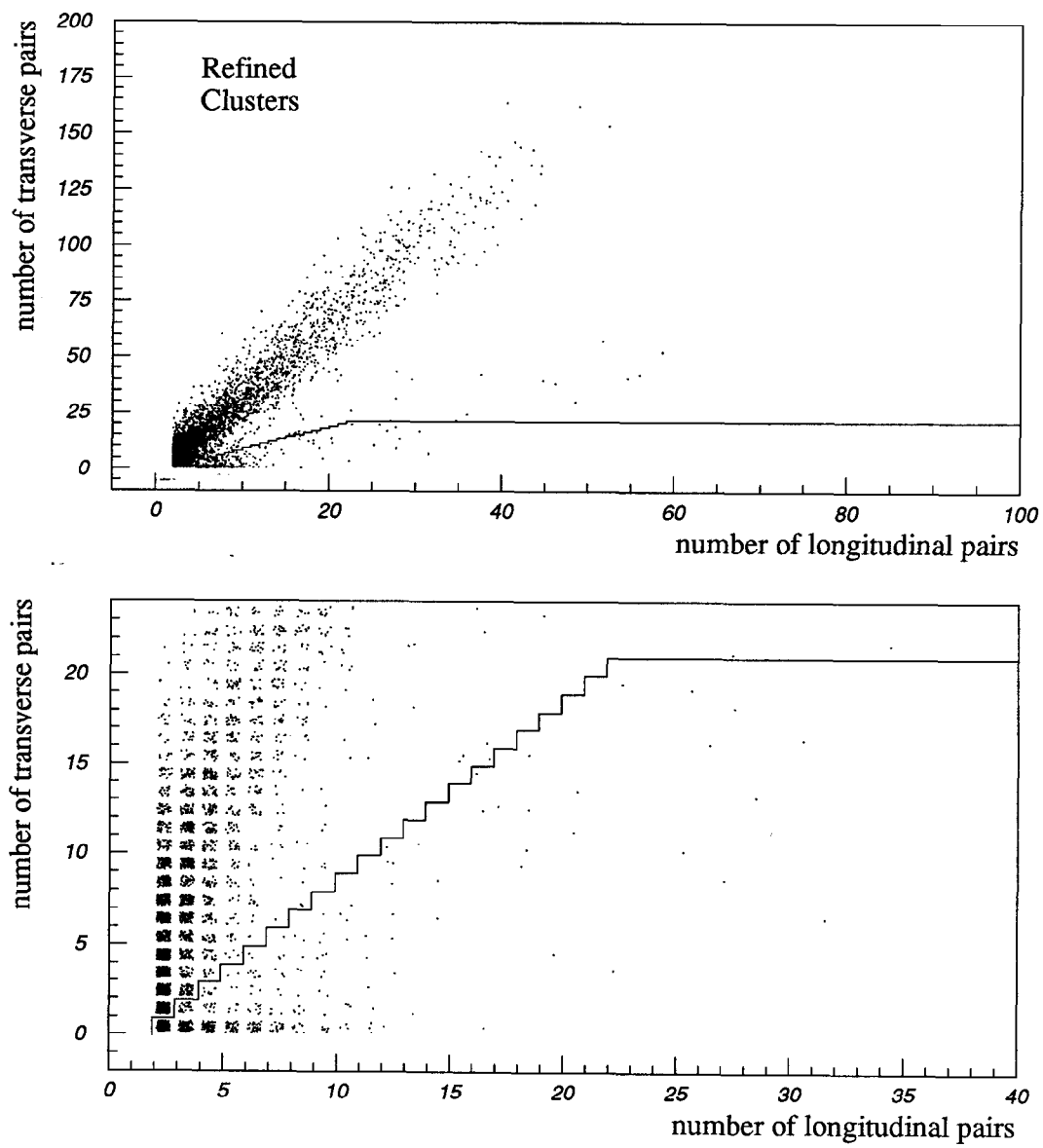
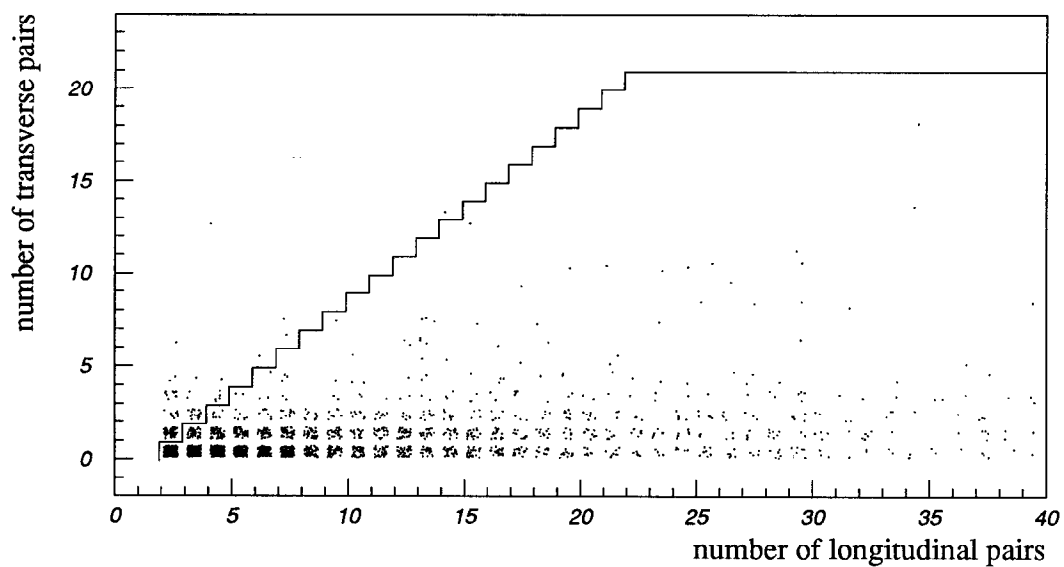
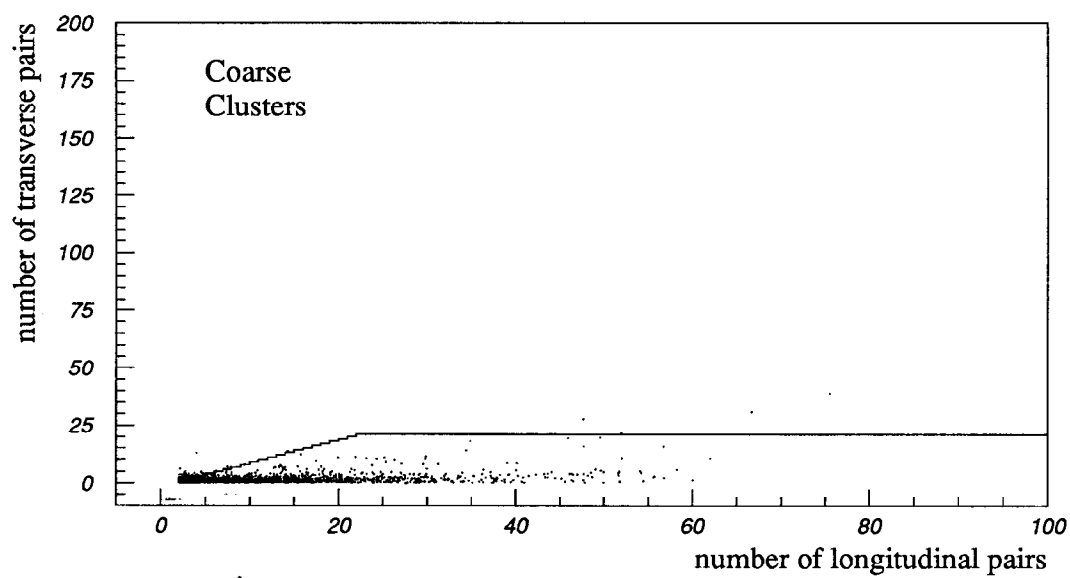


Figure A-1:  $n_t$  vs.  $n_l$  for coarse clusters for a loosely selected sample of hadronic events



**Figure A-2:**  $n_t$  vs.  $n_l$  for the refined clusters of those coarse clusters which were above the cuts.



**Figure A-3:**  $n_t$  vs.  $n_l$  for the coarse clusters in the small angle Bhabha events recorded by the LMSAT.

```

Run 13082, EVENT 5491
26-JUL-1992 01:34
Source: Run Data Pol: 0
Trigger: Energy CDC Hadron
Beam Crossing 2147297100

```

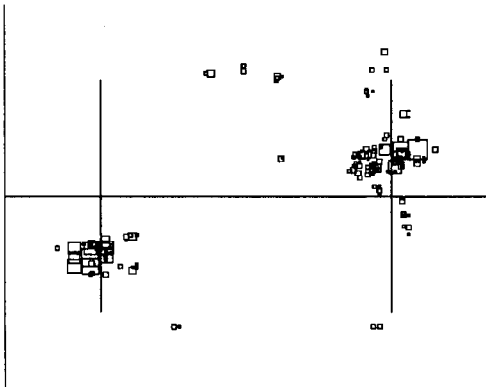


**Figure A-4:** A display of a hadronic event after SLC muon removal.

```

Run 13082, EVENT 5491
26-JUL-1992 01:34
Source: Run Data Pol: 0
Trigger: Energy CDC Hadron
Beam Crossing 2147297100

```

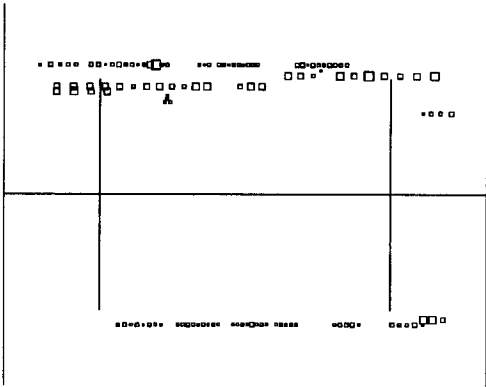


**Figure A-5:** A display of identified SLC muon induced clusters for the event displayed above.

# Bibliography

- [1] SLD collaboration: K. Abe et al. First Measurement of the Left-Right Cross Section Asymmetry in  $Z$  Boson Production by  $e^+e^-$  Collisions. *PRL*, 70(17):2515, 1993.
- [2] S.L. Glashow. Partial-Symmetries of Weak Interactions. *Nucl. Phys.*, 22:579, 1961.
- [3] S. Weinberg. A Model of Leptons. *PRL*, 19:1264, 1967.
- [4] A. Salam and J. C. Ward. Electromagnetic and Weak Interactions. *Phys. Lett.*, 13:168, 1964.
- [5] Particle Data Group. Review of Particle Properties. *Phys. Rev. D*, 45(11), 1992. Part II.
- [6] The LEP Collaborations and the LEP Electroweak Working Group. Updated Parameters of the  $Z^0$  Resonance from Combined Preliminary Data of the LEP Experiments. CERN/PPE/93-157, 1993.
- [7] M. Consoli and W. Hollik. Electroweak radiative corrections for  $Z$  physics. In *Z Physics at LEP 1*, page 7, 1989. CERN 89-08.
- [8] A. Blondel et al. Precision Measurements of Final State Weak Couplings from Polarized Electron-Positron Annihilation. *Nucl. Phys.*, B304:438, 1988.

- [9] U. Amaldi et al. Comprehensive Analysis of Data Pertaining to the Weak Neutral Current and the Intermediate-Vector-Boson masses. *Phys. Rev. D*, 36(5):1385, 1987.
- [10] M. Martinez and R. Miquel. Fitting the  $e^+e^- \rightarrow e^+e^-$  Lineshape. *Z. Phys. C*, 53:115, 1992.
- [11] SLD Collaboration: M.L. Swartz et al. First Measurement of the Left-Right  $Z$  Cross Section Asymmetry in Polarized  $e^+e^-$  Collisions at the SLC. SLAC-PUB-6034, 1993.
- [12] J. Kent et al. Precision Measurement of the SLC Beam Energy. SLAC-PUB-4922, 1989.
- [13] G. Blaylock. The WISRD Beam Energy Measurement. SLD Physics Note 22, 1993.
- [14] SLD Collaboration: M.J. Fero et al. The Compton Polarimeter for SLC. SLAC-PUB-6026, 1992.
- [15] SLD Design Report. SLAC-0273, 1984.
- [16] G.D. Agnew et al. Design and Performance of the SLD Vertex Detector, a 120 MPixel Tracking System. SLAC-PUB-5906, 1992.
- [17] L. Rochester et al. T. Markeiwics. Performance of the SLD Central Drift Chamber in the 1992 Physics Run. SLD Note 231, 1993.
- [18] Jan A. Lauber. SLAC-413, 1993. PhD Thesis.
- [19] M. Cavalli-Sforza et al. Construction and Testing of the SLD Cherenkov Ring Imaging Detector. SLAC-PUB-5123, 1990.
- [20] D. Axen et al. The Lead-Liquid Argon Sampling Calorimeter of the SLD. *NIM*, A328:472, 1993.

- [21] A.C. Benvenuti et al. The Limited Streamer Tubes of the SLD. *NIM*, A290:353, 1990.
- [22] S.C. Berridge et al. First Results from the SLD Silicon Calorimeter. *IEEE Trans. on Nucl. Sci.*, 39(5):1242, 1992.
- [23] S. Jadach et al. *Comp. Phys. Comm.*, 70:305, 1992.
- [24] F.A. Berends and R. Kleiss. *Nucl. Phys.*, B186:22, 1981.
- [25] Z. Was S. Jadach, B.F.L. Ward. *Comp. Phys. Comm.*, 66:276, 1991.
- [26] T. Sjöstrand. *Comp. Phys. Comm.*, 43:367, 1987.
- [27] R. Brun et al. GEANT3 User's Guide. CERN-DD/EE/84-1, 1989.
- [28] G. Grindhammer et al. *NIM*, A290:469, 1990.
- [29] E. Vella and J. Yamartino. Tower Thresholds for LAC Total Energy Trigger. SLD Note 213, 1992.
- [30] John M. Yamartino. Hadronic Event Selection Using the LAC. SLD Physics Note 14, 1992.
- [31] Saúl González. First-Pass Determination of the Energy Scale in the SLD Calorimeter. SLD Physics Note 24, 1993.
- [32] K.T. Pitts. Private Communication, 1993.
- [33] H. Band. Trigger Task Force Recommendations for Polarized Data Acquisition. SLAC Memorandum. May 12, 1993.
- [34] P.N. Burrows, H. Park, K.T. Pitts and J.M. Yamartino. Estimate of Combined Triggering and Selection Efficiency for Hadronic Events. SLD Note 229, 1993.
- [35] P. Raimondi. Private Communication, 1992.
- [36] K.T. Pitts. Luminosity Measurement for the 1992 Run. SLD Physics Note 20, 1993.



- [37] ALEPH Collaboration. Update of Electroweak Parameters from  $Z$  Decays. CERN-PPE/93-40, 1993. Submitted to *Z. Phys. C*.
- [38] DELPHI Collaboration. *Nucl. Phys.*, B367:511, 1991.
- [39] L3 Collaboration. Results from the L3 Experiment at LEP. CERN-PPE/93-31, 1993. Submitted to *Phys. Rep.*
- [40] OPAL Collaboration. Improved Measurements of the Neutral Current from Hadron and Lepton Production at LEP. CERN-PPE/93-146, 1993. Submitted to *Z. Phys. C*.
- [41] P. Comas and M. Martinez. Analyzing the  $e^+e^- \rightarrow e^+e^-$  Angular Distribution. *Z. Phys. C*, 58:15, 1993.
- [42] H. Park et al. Event Selection for the 1992  $A_{LR}$  Analysis. SLD Physics Note 17, 1993.